

Universal logical operations with a dynamical qubit in Floquet code

Xuandong Sun,^{1,2,3,*} Longcheng Li,^{4,5,*} Zhiyi Wu,^{6,2,*} Zechen Guo,^{1,2,3} Peisheng Huang,^{7,2} Wenhui Huang,^{1,2,3} Qixian Li,^{1,2,3} Yongqi Liang,^{1,2,3} Yiting Liu,^{1,2,3} Daxiong Sun,^{1,2,3} Zilin Wang,^{7,2} Changrong Xie,^{1,2,3} Yuzhe Xiong,^{1,2,3} Xiaohan Yang,^{1,2,3} Jiajian Zhang,^{1,2,3} Jiawei Zhang,^{1,2,3} Libo Zhang,^{1,2,3} Zihao Zhang,^{1,2,3} Weijie Guo,² Ji Jiang,^{1,2,3} Song Liu,^{1,2,3,8} Xiayu Linpeng,² Jingjing Niu,^{2,8} Jiawei Qiu,² Wenhui Ren,² Ziyu Tao,² Yuefeng Yuan,² Yuxuan Zhou,² Ji Chu,^{2,†} Youpeng Zhong,^{1,2,8,‡} Xiaoming Sun,^{4,5,§} and Dapeng Yu^{2,8,¶}

¹*Shenzhen Institute for Quantum Science and Engineering, Southern University of Science and Technology, Shenzhen 518055, China*

²*International Quantum Academy, Shenzhen 518048, China*

³*Guangdong Provincial Key Laboratory of Quantum Science and Engineering, Southern University of Science and Technology, Shenzhen 518055, China*

⁴*Institute of Computing Technology, Chinese Academy of Sciences, Beijing, China*

⁵*CAS Center for Excellence in Topological Quantum Computation, University of Chinese Academy of Sciences, Beijing, China*

⁶*School of Physics, Peking University, Beijing 100871, China*

⁷*School of Physics, Ningxia University, Yinchuan 750021, PR China*

⁸*Shenzhen Branch, Hefei National Laboratory, Shenzhen 518048, China*

(Dated: March 7, 2025)

Quantum error correction (QEC) protects quantum systems against inevitable noises and control inaccuracies, providing a pathway towards fault-tolerant (FT) quantum computation. However, the significant overhead of physical qubits required to encode a single logical qubit poses a major challenge for scalability and practical implementation. Floquet QEC codes, a recent innovation, mitigate this challenge by utilizing time-periodic measurements to introduce additional dynamical logical qubits, thereby enhancing resource efficiency in QEC. Here, we experimentally implement the Floquet-Bacon-Shor code on a superconducting quantum processor. We encode a dynamical logical qubit within a 3×3 lattice of data qubits, alongside a conventional static logical qubit. We demonstrate FT encoding and measurement of the two-qubit logical states and stabilize the states using repeated error detection cycles. Additionally, we showcase universal single-qubit logical gates on the dynamical qubit. By implementing a logical CNOT gate, we entangle the dynamical and static logical qubits, generating an error-detected logical Bell state with a fidelity of 75.9%. Our results highlight the potential of Floquet codes for scalable and resource-efficient FT quantum computation.

I. INTRODUCTION

Quantum computers hold potential for solving computational problems that are provably intractable for classical systems, with transformative applications in quantum simulation [1], cryptography [2], and machine learning [3]. However, their practical realization is hindered by a fundamental challenge: quantum information is inherently fragile, susceptible to inevitable environmental noise and control inaccuracies. To address this challenge, quantum error correction (QEC) has emerged as a critical framework [4–6]. By redundantly encoding logical qubits into larger systems with many physical qubits, QEC detects and corrects errors through repeated syndrome measurements. Combined with fault-tolerant (FT) logical operations, QEC not only safeguards quantum information, but also lays the foundation for scalable and reliable quantum computation.

A variety of QEC codes have been proposed, including surface code [7], color code [8], Bacon-Shor (BS) code [9], and quantum LDPC codes [10, 11]. Significant experimental progresses have been achieved in recent years across various platforms [12–21]. Notably, exponential error suppression has been demonstrated by scaling up a surface-code logical qubit using superconducting circuits [22]. While high-performance logical qubits can be realized by increasing the size of quantum processors, the code rate—the ratio of logical qubits to physical qubits—remains a crucial metric [11]. Low encoding efficiency can make FT quantum computing resource-intensive, especially for solid-state quantum devices limited to nearest-neighbor coupling.

Recently proposed time-dynamical QEC, including Floquet codes [23, 24] and generalized time-dynamical code implementations [25–29], opens up new opportunities for fault-tolerant quantum computation. A recent work [30] has shown the flexibility in surface code realization using time-dynamical implementations. Unlike conventional stabilizer or subsystem codes that encode logical information in a fixed subspace, the Floquet codes allow logical information to evolve periodically over time. Additional dynamical logical qubits are encoded through an appropriate measurement schedule, thereby improv-

* These authors contributed equally to this work.

† jichu@iqasz.cn

‡ zhongyp@sustech.edu.cn

§ sunxiaoming@ict.ac.cn

¶ yudapeng@iqasz.cn

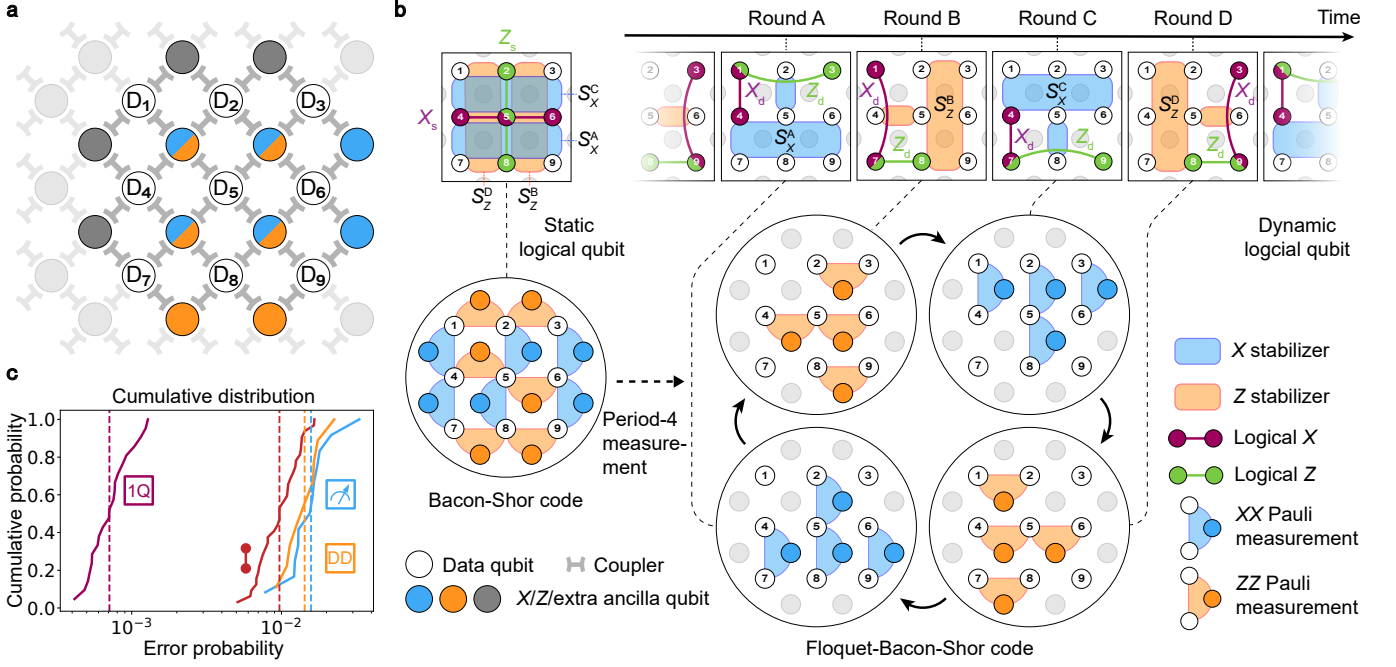


FIG. 1. **Implementation of the FBS code.** **a**, Schematic of the quantum device for the FBS code, consisting of 9 data qubits (white circles labeled as D_i , where $i = 1$ to 9) and 12 ancilla qubits (orange circles for Z ancillas and blue circles for X ancillas). The four central qubits are alternately used as X and Z ancillas in different stabilizer rounds. Extra ancilla qubits (grey circles) are used for circuit compression and the construction of logical CNOT gate. Each pair of qubits is connected by a tunable coupler (H shape). **b**, Illustration of stabilizer measurements for the BS code (left) and the FBS code (right). The FBS code features period-4 stabilizer measurements with evolving logical operators X_d (purple lines) and Z_d (green lines) for the dynamical qubit in different rounds. In contrast, the logical operators X_s and Z_s are fixed and identical for both codes. Weight-2 Pauli measurements are used to check the parity of the corresponding data qubits in the X (blue) and Z (orange) bases. **c**, Cumulative distributions of errors for simultaneous single-qubit gates, CZ gates, ancilla qubit readout, and data qubit idle (with dynamical decoupling) during ancilla readout are depicted. The median error rates are 0.07%, 0.97%, 1.58%, and 1.43%, respectively, as indicated by the vertical lines.

ing the code rate. During the periodic schedule of Pauli measurements, logical subspaces and operators adapt to stabilizer measurements while preserving the encoded information. Despite extensive theoretical study since its inception [31–46], the Floquet code has not yet been experimentally demonstrated.

In this work, we implement the Floquet-Bacon-Shor (FBS) code [42] on a superconducting quantum processor, encoding one conventional static logical qubit and one dynamical logical qubit simultaneously within a 3×3 array of data qubits. We demonstrate FT encoding and measurement of the two-qubit logical states, and stabilize these states using multi-round stabilizer measurements. We showcase FT Pauli gates and non-fault-tolerant (nFT) arbitrary rotation gates on the dynamical qubit. Furthermore, we achieve a logical Bell state fidelity of 75.9% by entangling the dynamical and static logical qubits via a logical CNOT gate, with the gate fidelity assessed at 84.1% through logical quantum process tomography (LQPT). With these demonstrated universal two-qubit logical operations, our results highlight the potential of Floquet codes for scalable and resource-efficient QEC.

II. RESULTS

The FBS code we demonstrate is a generalization of the $[[9, 1, 3]]$ BS code [9], a subsystem code that encodes one logical qubit on a 3×3 square lattice, as illustrated in Fig. 1a. Each vertex represents a data qubit, and each edge corresponds to a weight-2 Pauli measurement. The static logical qubit is encoded in a fixed subsystem, with its logical Pauli operators given by

$$X_s = X_4 X_5 X_6, \quad Z_s = Z_2 Z_5 Z_8, \quad Y_s = i X_s Z_s. \quad (1)$$

The BS code can be stabilized in a single measurement round using only weight-2 Pauli measurements, whose ordering is inconsequential [9], as shown in Fig. 1b. The four weight-6 stabilizers, S_X^A , S_Z^B , S_X^C , and S_Z^D , are derived by multiplying the outcomes of the corresponding Pauli measurements, enabling the detection and subsequent correction of any single-qubit error. Since these Pauli measurements do not always commute, the Hilbert space of the 9 physical qubits consists of 4 degrees of freedom fixed by the stabilizers, 1 degree for logical information, and 4 additional degrees corresponding to the

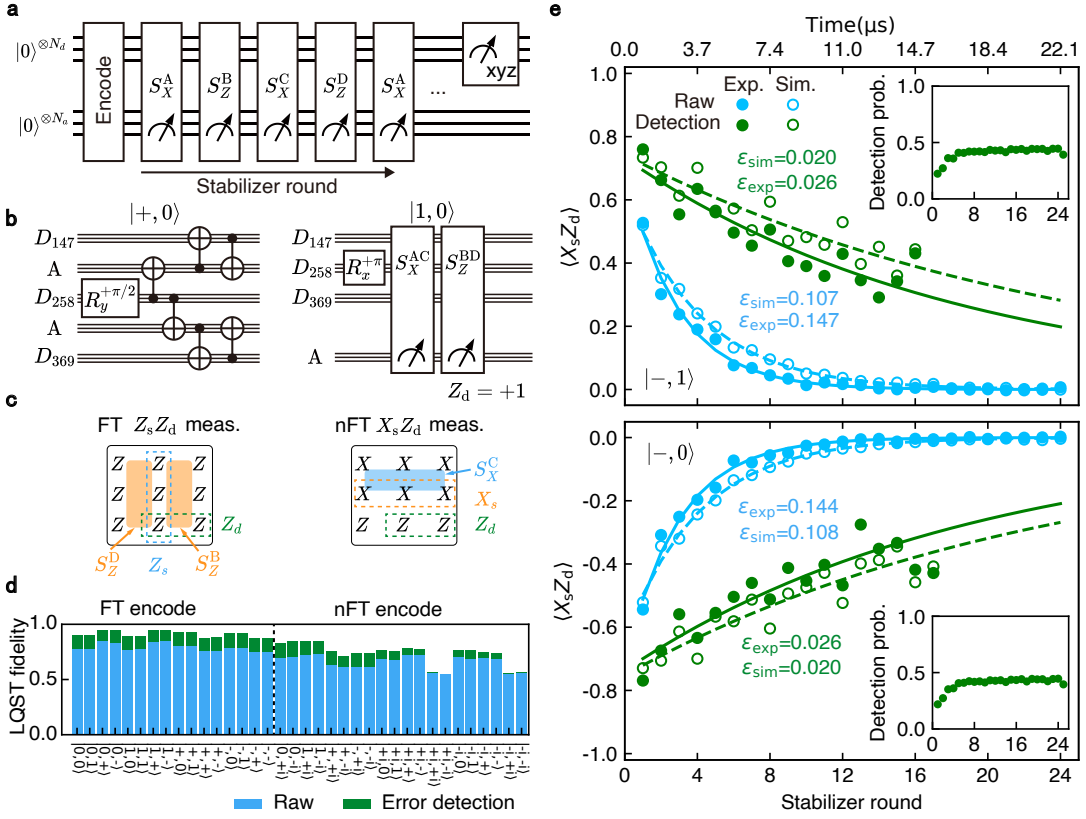


FIG. 2. **Encoding, stabilization, and measurement of two-qubit logical states in the FBS code.** **a**, Simplified circuit for encoding, stabilizing and measuring two-qubit logical states. All physical qubits are initialized to the ground state before the circuit. Period-4 stabilizer measurements are alternately performed following the encoding circuit. **b**, Encoding circuits for logical Pauli states $|+, 0\rangle$ and $|1, 0\rangle$. BS stabilizer measurements are included in the latter case, with the dynamical qubit state post-selected to be $|0\rangle$. **c**, Example logical measurement circuits after stabilizer S_Z^D : FT ZZ measurement (left) and nFT XZ measurement (right). Logical operators are indicated within the dashed-line boxes. Measurement outcomes of some data qubits are used to calculate the values of the X (blue) and Z (orange) stabilizers, enabling error detection. **d**, LQST fidelities of all 36 two-qubit Pauli states. The 16 states $\{|0\rangle, |1\rangle, |+\rangle, |-\rangle\}^{\otimes 2}$ are fault-tolerantly prepared and exhibit higher fidelity, as shown to the left of the dashed line. The blue portions indicate the fidelities without error detection, while the green portions highlight the fidelity improvement with error detection in the logical measurement. **e**, Experimentally measured (filled symbols) and simulated (open symbols) expectation values of $X_s Z_d$ operator versus stabilizer round, for the encoded states $|-, 1\rangle$ (top) and $|-, 0\rangle$ (bottom). The solid and dashed lines represent exponential fits. Each stabilizer round lasts 920 ns, comprising 720 ns for readout pulses and resonator photon depletion, and 200 ns for single-qubit and two-qubit gates. The cyan and green colors correspond to data without post-processing and data with measured error syndromes post-selected out, respectively. Due to the exponential decrease in the retained data during error detection, the analysis is limited to 16 rounds, with a total of 100,000 experimental shots. The insets show the error detection probabilities for the weight-6 stabilizers over 24 measurement rounds, with the final round calculated from the logical measurements.

gauge space, which does not encode logical information. By imposing a period-4 ordering on the weight-2 Pauli measurements, the gauge space dynamically encodes an additional logical qubit, thereby forming the FBS code. In each round, 4 weight-2 Pauli measurements are performed, whose outcomes determine one weight-6 stabilizer and also influence the evaluation of dynamical operators (see Methods). The logical Pauli operators X_d and Z_d of the dynamically encoded qubit evolve periodically during the stabilizer measurements, as indicated by the purple and green lines in Fig. 1b. Both the static and dynamical logical qubits are stabilized over the 4 measurement rounds. Although the 3×3 system size is in-

sufficient for error correction of the dynamical qubit, the stabilizers extracted from the measurements are sufficient to detect any single-qubit error. Within the framework of error detection, an operation is considered FT if any single-qubit error produces a non-trivial syndrome and is thereby detectable [47].

We implement the FBS code on a superconducting quantum processor comprising a 6×11 array of Transmon qubits [48], each coupled to its four nearest neighbors through tunable couplers [49]. The experimental setup and device parameters are detailed in Supplementary Information Section II. The static and dynamical logical qubits are encoded on a 21-qubit subset of the

processor, consisting of $N_d = 9$ data qubits and $N_a = 12$ ancilla qubits. The data qubits, labeled as D_i ($i = 1$ to 9), form a 3×3 array and are interlaced with X and Z ancilla qubits for stabilizer measurements. Additional ancilla qubits are incorporated to optimize the QEC circuits. High-fidelity quantum gates and quantum non-demolition (QND) readout [50] are implemented on the 21-qubit subset, with the cumulative distributions of errors illustrated in Fig. 1c. The readout fidelities of the ancilla qubits are benchmarked using repeated measurements [51] (see Supplementary Information Section III). Dynamical decoupling (DD) techniques [52] are employed to protect the data qubits from low-frequency noise and cross-measurement-induced dephasing [53–55]. The idle errors (with DD) on the data qubits during ancilla qubit readout are quantified using interleaved randomized benchmarking [56].

The simplified circuit for logical state encoding, period-4 stabilization, and logical measurement is shown in Fig. 2a. Prior to the circuit, all ancilla qubits are reset to the ground state using an active protocol [57], while the data qubits are reset using a passive protocol [58]. We encode all 36 logical Pauli eigenstates $\{|0\rangle, |1\rangle, |+\rangle, |-\rangle, |+\rangle, |-\rangle, |+\rangle, |-\rangle\}^{\otimes 2}$ of the static and dynamical qubits. Among these states, the states $\{|0\rangle \otimes |+\rangle, |1\rangle \otimes |+\rangle, |+\rangle \otimes |0\rangle, |-\rangle \otimes |0\rangle\}$ (where the first ket corresponds to the static qubit and the second to the dynamical qubit) are equivalent to the states $\{|0\rangle, |1\rangle, |+\rangle, |-\rangle\}$ in the BS code, with specific states prepared in the gauge space. These logical states are products of three Greenberger–Horne–Zeilinger (GHZ) states [12], created in parallel using sequences of physical CNOT gates. An example circuit for state $|+\rangle, |0\rangle = |+\rangle \otimes |0\rangle$ is shown in Fig. 2b. The encoding circuit is FT because there are no entangling operations between the GHZ states that would allow errors to propagate. Other states in the set $\{|0\rangle, |1\rangle, |+\rangle, |-\rangle\}^{\otimes 2}$ are prepared by projecting the system onto the logical space via BS stabilizer measurements and post-selecting the states of the dynamical qubit, as illustrated in the encoding circuit for $|1, 0\rangle$. This encoding is also FT, as any single-qubit error in the encoding circuit will flip the stabilizer values computed from the BS stabilizer measurements, making such errors detectable. Two-qubit states involving $|\pm i\rangle$ are prepared in a nFT manner, as detailed in Supplementary Information Section VI.

Logical measurements are performed by measuring the data qubits in their appropriate bases, as illustrated by the example circuits in Fig. 2c. The measurement circuits for the dynamical qubit change according to the logical operator definitions in different stabilizer rounds. The outcome of a logical operator is determined by calculating the total parity of the relevant data qubits (see Methods). Data qubits that do not define the logical operators are also measured to enable error detection. The $Z_s Z_d$ measurement is FT because the measured outcomes allow for the calculation of stabilizers S_Z^D and S_Z^B , enabling the detection of any single-qubit error. In contrast, the

measurement of $X_s Z_d$ is nFT; however, the value of stabilizer S_X^C can be calculated from the measurement outcomes to detect phase-flip errors and measurement errors on qubits D_1 through D_6 . We present measured fidelities of the 36 encoded states in Fig. 2d. The state fidelities are determined using logical quantum state tomography (LQST), where 9 logical bases $\{Z, X, Y\}^{\otimes 2}$ are measured (see Methods for details on LQST and Supplementary Information Section VI for full measurement circuits). Error detection during the logical measurements improves the state fidelities, as indicated by the green portions in the plot.

We perform period-4 stabilizer measurements to preserve the encoded two-qubit logical states. Specifically, the four stabilizers $S_X^A, S_Z^B, S_X^C,$ and S_Z^D are alternately performed to detect bit-flip or phase-flip errors in both the static and dynamical qubits. Each measurement result is compared to the result of the same stabilizer type from four rounds earlier, with the first four rounds compared to the encoding value. Errors during this process manifest as changes in the measurement outcomes, and the corresponding data are post-selected out in error detection. We present the preservation results for the encoded states $|-, 0\rangle$ and $|-, 1\rangle$ in Fig. 2e, showing the measured expectation values of the operator $X_s Z_d$. The logical error rates (ε_{exp}) for these states, extracted by fitting the exponential decay of the expectation values, are reduced from 14.7% and 14.3% to 2.6% and 2.5%, respectively. This improvement corresponds to an increase in the logical lifetime $T_L = \tau_{\text{exp}}/2\varepsilon_{\text{exp}}$ from 3.1 μs and 3.2 μs to 17.7 μs and 18.4 μs [17], respectively. Here, $\tau_{\text{exp}} = 920$ ns is the duration of a stabilizer round. Numerical simulation results using the open-source package Stim [59], based on monitored gate and measurement errors, are also shown for comparison. The larger error rates observed in experiments may arise from leakage-induced correlated errors [54, 58, 60–64]. We measure an average leakage rate of 0.18% per round on the physical qubits using three-state readout at the end of the circuit (see Supplementary Information IV). In both the experimental and simulation data, round-dependent oscillations are observed. Specifically, higher expectation values occur every four rounds, corresponding to the completion of a full error detection cycle. Beyond error detection, error correction can be applied to the static qubit alone (see Supplementary Information VI). However, the effectiveness of error correction diminishes for the two-qubit states due to the small code distance of the dynamical qubit and the correlation between errors in the two logical qubits.

We demonstrate universal logical gates on the dynamical qubit, including FT Pauli gates and nFT arbitrary rotation gates. For logical gates on the static qubit, see Supplementary Information Section V and reference [12]. The Pauli gates are implemented transversally using parallel single-qubit gates on the corresponding data qubits, as defined by the logical operators. We insert the Pauli gates $\{I_s \otimes X_d, I_s \otimes Y_d, I_s \otimes Z_d\}$ between the stabi-

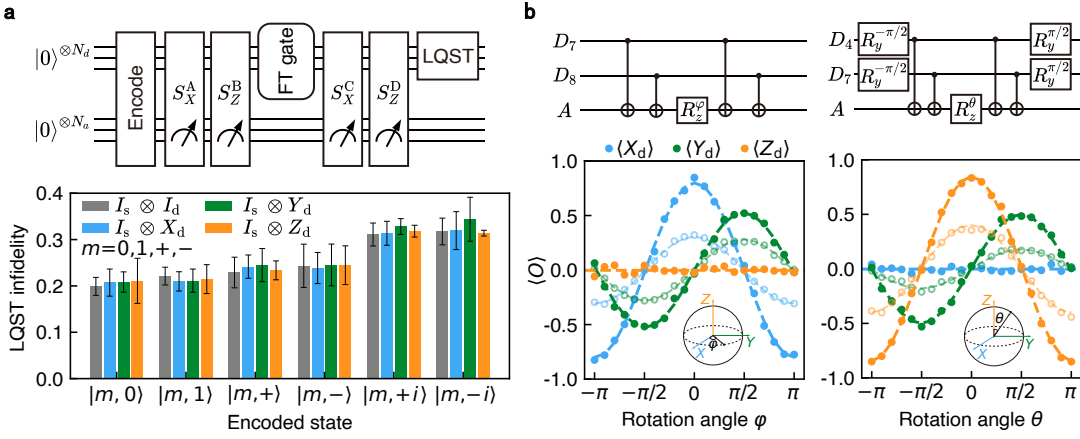


FIG. 3. **Logical gates on the dynamical qubit.** **a**, FT Pauli gates on the dynamical qubit. Transversal Pauli gates are applied to the data qubits and inserted between stabilizers S_Z^B and S_X^C , as shown at the top. The final state is characterized using LQST. The state infidelities with error detection after applying the Pauli gates on different encoded states are shown below the circuit. For each dynamical qubit state, the infidelity is averaged over 4 static qubit states $\{|0\rangle, |1\rangle, |+\rangle, |-\rangle\}$. Error bars correspond to 95% confidence intervals. **b**, Logical rotation gates on the dynamical qubit around the Z_d -axis (left) and X_d -axis (right). The measurement expectation values of the operators X_d (cyan), Y_d (green) and Z_d (orange) are shown as functions of rotation angles φ and θ . The gate circuits (shown at the top) for rotations around the Z_d -axis (X_d -axis) are inserted between stabilizers S_Z^B (S_X^C) and S_X^C (S_Z^D). The filled (open) symbols represent data with (without) error detection in the four stabilizer rounds and the final logical measurement. The dashed curves correspond to trigonometric fits.

lizers S_Z^B and S_X^C , as illustrated in Fig 3a. The final states, after applying the gates and conducting four stabilizer rounds, are characterized using LQST. For each encoded Pauli state of the dynamical qubit, the static qubit traverses four states: $\{|0\rangle, |1\rangle, |+\rangle, |-\rangle\}$. The average state infidelities after applying the gates $I_s \otimes X_d$, $I_s \otimes Y_d$, and $I_s \otimes Z_d$ are 0.255 ± 0.011 , 0.263 ± 0.013 , and 0.256 ± 0.011 , respectively. These values are close to the infidelity 0.253 ± 0.011 observed for the identity operation (i.e., no gates inserted), indicating that the FT Pauli gates induce negligible errors.

The construction of arbitrary rotation gates is facilitated by the use of ancilla qubits. For logical rotations around the Z_d -axis (R_Z^φ), a physical gate R_z^φ is inserted on an ancilla qubit and placed between four physical CNOT gates acting on D_7 and D_8 , as illustrated at the top of Fig. 3b. The entire circuit is then inserted between stabilizers S_Z^B and S_X^C . Similarly, logical rotations around the X_d -axis (R_X^θ) are implemented using an R_x^θ gate on an ancilla qubit. The corresponding circuit is inserted between stabilizers S_X^C and S_Z^D . We sweep the rotation angles φ and θ and measure the dynamical qubit in three bases: X_d , Y_d , and Z_d . The measurement results are shown in Fig. 3b, with filled (open) symbols representing data with (without) error detection. With error detection enabled, the lower amplitude in the Y_d -direction is primarily due to the nFT nature of the logical Y_d measurement. Without error detection, the amplitude in the Y_d -direction is lower than that in the Z_d -direction for the R_X^θ rotation due to more phase-flip errors propagating through the nFT R_X^θ gate.

Finally, we show that the dynamical and static qubits can be entangled using a logical CNOT gate. The specific

CNOT circuit depends on the preceding stabilizer type. In our implementation, the CNOT circuit is inserted between stabilizers S_Z^B and S_X^C . This circuit involves 14 entangling gates acting on a subgroup of 3 data qubits and 2 ancilla qubits, as illustrated in Fig. 4a. The circuit is derived from using the static qubit operator $Z_s = Z_1 Z_4 Z_7$ (which is equivalent to Z_s in Eq. 1 up to stabilizer S_Z^D) to control the dynamical qubit operator $X_d = X_1 X_7$ after round S_Z^B (see Supplementary Information Section I for theoretical derivation). We note that the logical CNOT gate we implement is nFT because it allows errors to propagate between the 3 involved data qubits. The circuit is intentionally designed to involve only 3 data qubits to minimize error propagation.

Applying the logical CNOT gate to the encoded state $|+, 0\rangle$ yields a logical Bell state $\frac{1}{\sqrt{2}}(|0, 0\rangle + |1, 1\rangle)$. The error-detected logical density matrix ρ_B is depicted in Fig. 4b, with a fidelity of 75.9%. Without error detection, the corresponding fidelity is only 38.8%. We benchmark the logical CNOT gate fidelity using LQPT. 16 linearly independent two-qubit logical states $\{|0\rangle, |1\rangle, |-\rangle, |-\rangle\}^{\otimes 2}$ are prepared in the encoding process. For each initial state, two-qubit LQST is performed at the end of the circuit. Due to the susceptibility of LQPT to state preparation and measurement (SPAM) errors, we characterize the input states using the same circuit without inserting the logical CNOT gate [65]. The logical Pauli transfer matrix (LPTM) R_{exp} , which linearly matches the input states to output states, is calculated using the 16 input-output pairs (see Methods). The resulting LPTM with error detection is shown in Fig. 4b. The process fidelity is calculated by comparing R_{exp} with the ideal transfer matrix R_{ideal} , yielding

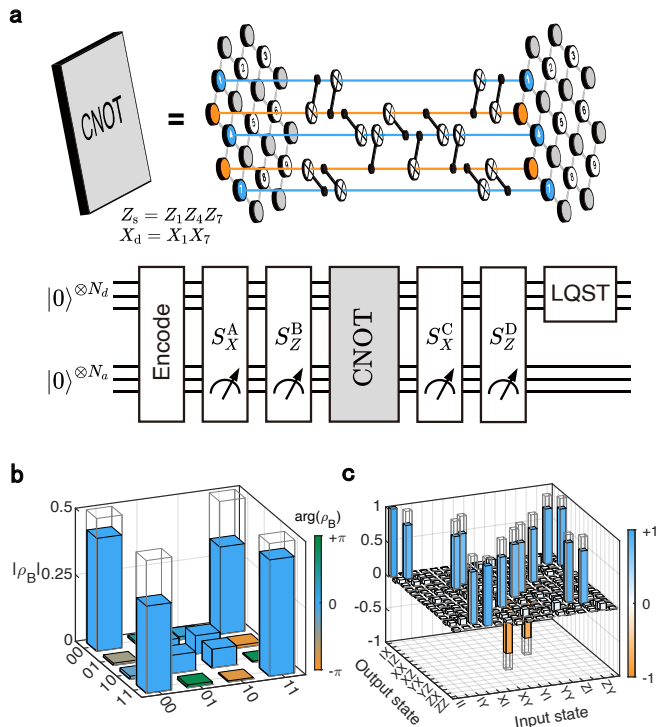


FIG. 4. **Logical CNOT gate between the dynamical and static qubits.** **a**, The CNOT circuit (top) is inserted between stabilizers S_Z^B and S_X^C in the overall circuit (bottom). For Bell state generation, the logical qubits are initialized to $|+, 0\rangle$ in the encoding process. For LQPT, 16 linearly independent logical cardinal states: $\{|0\rangle, |1\rangle, |-\rangle, |-i\rangle\}^{\otimes 2}$ are encoded. **b**, Error-detected logical density matrix of the generated logical Bell state, obtained with four stabilizer rounds. The logical state fidelity is 75.9% with error detection and 38.8% without error detection. **c**, Extracted LPTM R_{exp} of the CNOT gate, with a process fidelity $F_p = 80.2\%$.

$\mathcal{F}_p = \text{Tr}(R_{\text{exp}} \cdot R_{\text{ideal}}) = 80.2\%$. This corresponds to a gate fidelity $\mathcal{F}_g = (\mathcal{F}_p/E + 1)/(E + 1)$ of 84.1%, where $E = 4$ is the Hilbert space dimension. The fidelity calculation based on LQPT suffers from the low fidelity of encoded $|-i\rangle$ state on either qubit. We can also estimate the logical CNOT gate fidelity by dividing the average output state fidelity by the average input state fidelity without $|-i\rangle$, indicating a gate fidelity of 93.6%.

III. DISCUSSION AND OUTLOOK

In this work, we implement the FBS code on a superconducting quantum processor, encoding a dynamical logical qubit in addition to a conventional static logical qubit. We experimentally demonstrate universal two-qubit logical operations integrated with repetitive quantum error detection, including encoding, measurement, arbitrary single-qubit rotations, and a CNOT gate. Some of these logical operations are implemented in a FT manner and outperform their nFT counterparts. Our first

demonstration of universal logical operations with a dynamical logical qubit highlights the significant role played by Floquet codes in achieving resource-efficient FT quantum computation.

There are several challenges that remain for future work: (1) Despite improvements in code rate using the FBS code, our experiments show that the dynamical logical qubit is more susceptible to errors, requiring a larger code distance for effective protection. Specifically, the code distance for the dynamical qubit is approximately $d/2$ when the FBS code is implemented on a $d \times d$ square lattice [42]. Further research is needed to scale up the FBS code to larger lattices to enable effective error correction for the dynamical qubit. (2) Implementing FT entanglement and non-Clifford gates with the dynamical logical qubit is a critical next step. It has been shown that standard methods used in surface code, such as lattice surgery [24] and braiding twist defects [38], can be adapted to Floquet codes. A recent theoretical work has explored FT logical operations using a generalized Floquet code in a honeycomb lattice, demonstrating that entanglement operations can be achieved by simply re-ordering the measurement schedule [66]. This suggests that Floquet codes may offer a simpler and more natural pathway to FT quantum computing.

IV. METHODS

A. Logical operator definition in the FBS code

The FBS code is derived from its parent subsystem code, the $[[9, 1, 3]]$ BS code, which employs a 3×3 square lattice of data qubits to encode one logical qubit. The gauge group G of the BS code is generated by the following 12 weight-2 gauge operators (refer to Fig. 1a for qubit numbering):

$$\langle Z_1 Z_2, Z_2 Z_3, Z_4 Z_5, Z_5 Z_6, Z_7 Z_8, Z_8 Z_9, \\ X_1 X_4, X_2 X_5, X_3 X_6, X_4 X_7, X_5 X_8, X_6 X_9 \rangle.$$

By identifying the operators in G that commute with all elements in G , we obtain 4 weight-6 stabilizers:

$$S_X^A = X_4 X_5 X_6 X_7 X_8 X_9, \quad S_Z^B = Z_2 Z_3 Z_5 Z_6 Z_8 Z_9, \\ S_X^C = X_1 X_2 X_3 X_4 X_5 X_6, \quad S_Z^D = Z_1 Z_2 Z_4 Z_5 Z_7 Z_8.$$

The values of the above stabilizers can be obtained by measuring all 12 gauge operators and multiplying the corresponding measurement outcomes. By identifying the operators that commute with all elements in G but are not themselves in G , we obtain the logical operators of the static logical qubit, as defined in Eq. 1.

The FBS code is constructed by measuring the gauge operators in a period-4 schedule (see Fig. 1b), thereby encoding an additional dynamical logical qubit. Up to a ± 1 sign, the logical operator of the dynamical qubit evolves according to the period-4 schedule, as shown in

Table I. In the remainder of this section, we omit the superscript “Q” if it is clear from the context. For Pauli

TABLE I. Expressions for *unsigned* dynamical logical operators.

Round Q	A	B	C	D
X_d^Q	X_1X_4	X_1X_7	X_4X_7	X_3X_9
Z_d^Q	Z_1Z_3	Z_7Z_8	Z_7Z_9	Z_8Z_9
Y_d^Q	$Y_1Z_3X_4$	$X_1Y_7Z_8$	$X_4Y_7Z_9$	$X_3Z_8Y_9$

operators $P \in \{X, Y, Z\}$, the sign at round r is given by formula $\Gamma_P^{(r)} = \prod_{i=1}^r \gamma_P^{(i)}$, where $\gamma_P^{(i)}$ is defined in Table II. Combining all of the above, the logical P operator of the dynamical qubit at round r is given by $P_d^{(r)} = \Gamma_P^{(r)} P_d^Q$, where $Q = A, B, C, D$ for $r \equiv 1, 2, 3, 0 \pmod{4}$, respectively.

TABLE II. **Definition of $\gamma_X^{(i)}, \gamma_Z^{(i)}, \gamma_Y^{(i)}$.** At round i , $x_{uv}^{(i)}, z_{uv}^{(i)} \in \{\pm 1\}$ denotes the ancilla measurement outcome of weight-2 Pauli operators X_uX_v and Z_uZ_v . $S_X^A, S_Z^B, S_X^C, S_Z^D \in \{\pm 1\}$ refer to the initial values of the stabilizers determined by the encoding process.

$i \pmod{4}$	1	2	3	0
$\gamma_X^{(i)}$	$x_{69}^{(i)} x_{25}^{(i)} S_X^C$	$x_{47}^{(i-1)}$	$x_{14}^{(i)}$	$x_{36}^{(i-1)} x_{58}^{(i-1)} S_X^A$
$\gamma_Z^{(i)}$	$z_{12}^{(i-1)} z_{56}^{(i-1)} S_Z^B$	$z_{23}^{(i)} z_{45}^{(i)} S_Z^D$	$z_{89}^{(i-1)}$	$z_{78}^{(i)}$
$\gamma_Y^{(i)}$	$\gamma_X^{(i)} \gamma_Z^{(i)}$			

B. Logical operator evaluation using data-qubit measurement outcomes

For the static qubit, the logical operator is calculated from the measurement outcomes of data qubits during logical measurement. The values of the static logical operators are evaluated by multiplying the measurement outcomes of the corresponding data qubits, i.e., $X_s = x_4x_5x_6$, $Z_s = z_2z_5z_8$, $Y_s = x_4x_6y_5z_2z_8$, where $x_i, y_i, z_i \in \{\pm 1\}$ denote the X, Y , and Z measurement outcomes of data qubit D_i , respectively.

Assume the logical measurement is performed after r rounds of stabilizer measurement. For Pauli operator $P \in \{X, Y, Z\}$, the value of the dynamical logical operator $P_d^{(r)} = \Gamma_P^{(r)} P_d$ is the product of two parts: the value of its unsigned operator P_d and the value of its sign $\Gamma_P^{(r)}$ at round r . Similar to the static logical operators, the value of P_d is obtained by multiplying the measurement outcomes of the corresponding data qubits (see Table I). The value of $\Gamma_P^{(r)}$ is calculated as $\Gamma_P^{(r)} = \prod_{i=1}^r \gamma_P^{(i)}$, where $\gamma_P^{(i)}$ is determined by the ancilla measurement outcomes during encoding and stabilizer measurements (see Table II). Due to the presence of $\Gamma_P^{(r)}$, the evaluation of logical operators will change if we apply the logical rotation and

the CNOT gate described in the main text (see Supplementary Information Section I for theoretical details).

C. Two-qubit Logical Quantum State Tomography

The construction of the logical density matrix ρ_L in the Z basis follows a procedure similar to that used for a physical density matrix. For a physical density matrix, single-qubit gates $\{I, R_y^{\pi/2}, R_x^{\pi/2}\}$ are applied to the physical qubits before performing projective measurements, enabling measurements in the X, Y , and Z directions. However, for logical states, these rotation operations are unnecessary. Instead, we directly perform logical measurements in the X, Y , and Z bases. For a two-qubit logical state, we measure the state in 9 logical bases $\{Z, X, Y\}^{\otimes 2}$. For each basis, we obtain an array $[p_{--}, p_{-+}, p_{+-}, p_{++}]$, where p_{-+} denotes the probability of measuring the static qubit as -1 and the dynamical qubit as $+1$.

We optimize the logical density matrix ρ_L using the convex optimization package `cvxpy` [67], constraining the density matrix to be Hermitian, unit-trace and positive semi-definite. The fidelity of the reconstructed state relative to a target pure state is calculated as $\text{Tr}(\rho_L \rho_{\text{ideal}})$.

D. Two-qubit Logical Quantum Process tomography

LQPT is built upon the results of LQST. Each two-qubit logical density matrix ρ_L can be expressed in the two-qubit Pauli basis as a vector $\vec{p}^T = [p_{00}, p_{01}, \dots, p_{32}, p_{33}]$, where

$$p_{ij} = \frac{\text{Tr}(\rho_L \sigma_i \otimes \sigma_j)}{\text{Tr}(\rho_L)}, \text{ and } \sigma_i, \sigma_j \in \{I, X, Y, Z\}.$$

The LPTM R , a 16×16 matrix, maps an input state vector \vec{p} to an output state vector $\vec{p}' = R\vec{p}$ [68]. To reconstruct the LPTM, we employ convex optimization to find an optimal LPTM that satisfies all the constraints of a physical quantum channel, using an overcomplete set of input states.

Acknowledgements

We thank Bujiao Wu for valuable discussions. This work was supported by the Innovation Program for Quantum Science and Technology (2021ZD0301703), the Science, Technology and Innovation Commission of Shenzhen Municipality (KQTD20210811090049034), the National Natural Science Foundation of China (12174178, 12374474, 123b2071).

Author contributions

X.D.S. developed the FPGA program for custom electronics, collected and analyzed the data. L.C.L. conducted the theoretical analysis, supervised by X.M.S. Z.Y.W. and J.C. calibrated the quantum processor. J.C.

conceived the experiments. Y.P.Z. and D.P.Y. supervised the project. All authors contributed to the experimental setup, discussions of the results and writing of the manuscript.

Competing interests

The authors declare no competing interests.

Data availability

The data that support the plots within this paper and other findings of this study are available from the corresponding authors upon reasonable request.

-
- [1] Lloyd, S. Universal quantum simulators. *Science* **273**, 1073–1078 (1996).
- [2] Shor, P. W. Polynomial-time algorithms for prime factorization and discrete logarithms on a quantum computer. *SIAM Review* **41**, 303–332 (1999).
- [3] Biamonte, J. *et al.* Quantum machine learning. *Nature* **549**, 195–202 (2017).
- [4] Knill, E. & Laflamme, R. Theory of quantum error-correcting codes. *Physical Review A* **55**, 900 (1997).
- [5] Nielsen, M. A. & Chuang, I. L. *Quantum computation and quantum information* (Cambridge university press, 2010).
- [6] Terhal, B. M. Quantum error correction for quantum memories. *Reviews of Modern Physics* **87**, 307–346 (2015).
- [7] Kitaev, A. Y. Fault-tolerant quantum computation by anyons. *Annals of Physics* **303**, 2–30 (2003).
- [8] Bombin, H. & Martin-Delgado, M. A. Topological quantum distillation. *Physical Review Letters* **97**, 180501 (2006).
- [9] Bacon, D. Operator quantum error-correcting subsystems for self-correcting quantum memories. *Physical Review A—Atomic, Molecular, and Optical Physics* **73**, 012340 (2006).
- [10] Panteleev, P. & Kalachev, G. Asymptotically good quantum and locally testable classical ldpc codes. In *Proceedings of the 54th Annual ACM SIGACT Symposium on Theory of Computing*, 375–388 (2022).
- [11] Bravyi, S. *et al.* High-threshold and low-overhead fault-tolerant quantum memory. *Nature* **627**, 778–782 (2024).
- [12] Egan, L. *et al.* Fault-tolerant control of an error-corrected qubit. *Nature* **598**, 281–286 (2021).
- [13] Postler, L. *et al.* Demonstration of fault-tolerant universal quantum gate operations. *Nature* **605**, 675–680 (2022).
- [14] Paetznick, A. *et al.* Demonstration of logical qubits and repeated error correction with better-than-physical error rates. *arXiv preprint arXiv:2404.02280* (2024).
- [15] Pogorelov, I. *et al.* Experimental fault-tolerant code switching. *Nature Physics* 1–6 (2025).
- [16] Zhao, Y. *et al.* Realization of an error-correcting surface code with superconducting qubits. *Physical Review Letters* **129**, 030501 (2022).
- [17] Krinner, S. *et al.* Realizing repeated quantum error correction in a distance-three surface code. *Nature* **605**, 669–674 (2022).
- [18] Acharya, R. *et al.* Suppressing quantum errors by scaling a surface code logical qubit. *Nature* **614**, 676–681 (2023).
- [19] Lacroix, N. *et al.* Scaling and logic in the color code on a superconducting quantum processor. *arXiv preprint arXiv:2412.14256* (2024).
- [20] Bluvstein, D. *et al.* Logical quantum processor based on reconfigurable atom arrays. *Nature* **626**, 58–65 (2024).
- [21] Abobeih, M. H. *et al.* Fault-tolerant operation of a logical qubit in a diamond quantum processor. *Nature* **606**, 884–889 (2022).
- [22] Acharya, R. *et al.* Quantum error correction below the surface code threshold. *Nature* (2024).
- [23] Hastings, M. B. & Haah, J. Dynamically generated logical qubits. *Quantum* **5**, 564 (2021).
- [24] Haah, J. & Hastings, M. B. Boundaries for the honeycomb code. *Quantum* **6**, 693 (2022).
- [25] Gottesman, D. Opportunities and challenges in fault-tolerant quantum computation. *arXiv preprint arXiv:2210.15844* (2022).
- [26] McEwen, M., Bacon, D. & Gidney, C. Relaxing hardware requirements for surface code circuits using time-dynamics. *Quantum* **7**, 1172 (2023).
- [27] Gidney, C. & Jones, C. New circuits and an open source decoder for the color code. *arXiv preprint arXiv:2312.08813* (2023).
- [28] Delfosse, N. & Paetznick, A. Spacetime codes of clifford circuits. *arXiv preprint arXiv:2304.05943* (2023).
- [29] Shaw, M. H. & Terhal, B. M. Lowering connectivity requirements for bivariate bicycle codes using morphing circuits. *arXiv preprint arXiv:2407.16336* (2024).
- [30] Eickbusch, A. *et al.* Demonstrating dynamic surface codes (2024). 2412.14360.
- [31] Vuillot, C. Planar floquet codes. *arXiv preprint arXiv:2110.05348* (2021).

- [32] Gidney, C., Newman, M., Fowler, A. & Broughton, M. A fault-tolerant honeycomb memory. *Quantum* **5**, 605 (2021).
- [33] Zhang, Z., Aasen, D. & Vijay, S. X-cube floquet code: A dynamical quantum error correcting code with a subextensive number of logical qubits. *Physical Review B* **108**, 205116 (2023).
- [34] Aasen, D., Wang, Z. & Hastings, M. B. Adiabatic paths of hamiltonians, symmetries of topological order, and automorphism codes. *Physical Review B* **106**, 085122 (2022).
- [35] Davydova, M., Tantivasadakarn, N. & Balasubramanian, S. Floquet codes without parent subsystem codes. *PRX Quantum* **4**, 020341 (2023).
- [36] Townsend-Teague, A., de la Fuente, J. M. & Kesselring, M. Floquetifying the colour code. *arXiv preprint arXiv:2307.11136* (2023).
- [37] Sullivan, J., Wen, R. & Potter, A. C. Floquet codes and phases in twist-defect networks. *Physical Review B* **108**, 195134 (2023).
- [38] Ellison, T. D., Sullivan, J. & Dua, A. Floquet codes with a twist. *arXiv preprint arXiv:2306.08027* (2023).
- [39] Fahimniya, A. *et al.* Fault-tolerant hyperbolic floquet quantum error correcting codes. *arXiv preprint arXiv:2309.10033* (2023).
- [40] Paetznick, A. *et al.* Performance of planar floquet codes with majorana-based qubits. *PRX Quantum* **4**, 010310 (2023).
- [41] Aasen, D., Haah, J., Li, Z. & Mong, R. S. Measurement quantum cellular automata and anomalies in floquet codes. *arXiv preprint arXiv:2304.01277* (2023).
- [42] Alam, M. S. & Rieffel, E. Dynamical logical qubits in the bacon-shor code. *arXiv preprint arXiv:2403.03291* (2024).
- [43] Bauer, A. Topological error correcting processes from fixed-point path integrals. *Quantum* **8**, 1288 (2024).
- [44] Higgott, O. & Breuckmann, N. P. Constructions and performance of hyperbolic and semi-hyperbolic floquet codes. *PRX Quantum* **5**, 040327 (2024).
- [45] Hilaire, P. *et al.* Enhanced fault-tolerance in photonic quantum computing: Floquet code outperforms surface code in tailored architecture. *arXiv preprint arXiv:2410.07065* (2024).
- [46] Fu, X. & Gottesman, D. Error correction in dynamical codes. *arXiv preprint arXiv:2403.04163* (2024).
- [47] Tomita, Y. & Svore, K. M. Low-distance surface codes under realistic quantum noise. *Physical Review A* **90**, 062320 (2014).
- [48] Koch, J. *et al.* Charge-insensitive qubit design derived from the cooper pair box. *Physical Review A—Atomic, Molecular, and Optical Physics* **76**, 042319 (2007).
- [49] Yan, F. *et al.* Tunable coupling scheme for implementing high-fidelity two-qubit gates. *Physical Review Applied* **10**, 054062 (2018).
- [50] Braginsky, V. B. & Khalili, F. Y. Quantum nondemolition measurements: the route from toys to tools. *Reviews of Modern Physics* **68**, 1 (1996).
- [51] Hazra, S. *et al.* Benchmarking the readout of a superconducting qubit for repeated measurements. *arXiv preprint arXiv:2407.10934* (2024).
- [52] Bylander, J. *et al.* Noise spectroscopy through dynamical decoupling with a superconducting flux qubit. *Nature Physics* **7**, 565–570 (2011).
- [53] Heinsoo, J. *et al.* Rapid high-fidelity multiplexed readout of superconducting qubits. *Physical Review Applied* **10**, 034040 (2018).
- [54] Bultink, C. *et al.* Protecting quantum entanglement from leakage and qubit errors via repetitive parity measurements. *Science Advances* **6**, eaay3050 (2020).
- [55] Chen, Z. *et al.* Exponential suppression of bit or phase errors with cyclic error correction. *Nature* **595**, 383–387 (2021).
- [56] Magesan, E. *et al.* Efficient measurement of quantum gate error by interleaved randomized benchmarking. *Physical Review Letters* **109**, 080505 (2012).
- [57] Johnson, J. *et al.* Heralded state preparation in a superconducting qubit. *Physical Review Letters* **109**, 050506 (2012).
- [58] Yang, X. *et al.* Coupler-assisted leakage reduction for scalable quantum error correction with superconducting qubits. *Physical Review Letters* **133**, 170601 (2024).
- [59] Gidney, C. Stim: a fast stabilizer circuit simulator. *Quantum* **5**, 497 (2021).
- [60] Fowler, A. G. & Martinis, J. M. Quantifying the effects of local many-qubit errors and nonlocal two-qubit errors on the surface code. *Physical Review A* **89**, 032316 (2014).
- [61] McEwen, M. *et al.* Removing leakage-induced correlated errors in superconducting quantum error correction. *Nature communications* **12**, 1761 (2021).
- [62] Lacroix, N. *et al.* Fast flux-activated leakage reduction for superconducting quantum circuits. *arXiv preprint arXiv:2309.07060* (2023).
- [63] Miao, K. C. *et al.* Overcoming leakage in quantum error correction. *Nature Physics* **19**, 1780–1786 (2023).
- [64] Marques, J. *et al.* All-microwave leakage reduction units for quantum error correction with superconducting transmon qubits. *Physical Review Letters* **130**, 250602 (2023).
- [65] Marques, J. F. *et al.* Logical-qubit operations in an error-detecting surface code. *Nature Physics* **18**, 80–86 (2022).
- [66] Davydova, M., Tantivasadakarn, N., Balasubramanian, S. & Aasen, D. Quantum computation from dynamic automorphism codes. *Quantum* **8**, 1448 (2024).
- [67] Diamond, S. & Boyd, S. Cvxpy: A python-embedded modeling language for convex optimization. *Journal of Machine Learning Research* **17**, 1–5 (2016).
- [68] Chow, J. M. *et al.* Universal quantum gate set approaching fault-tolerant thresholds with superconducting qubits. *Physical Review Letters* **109**, 060501 (2012).

Supplementary Information for “Universal logical operations with a dynamical qubit in Floquet code”

CONTENTS

I. Logical CNOT gate and rotation gates in the Floquet-Bacon-Shor code	2
A. Construction of the logical CNOT gate	2
B. Construction of the logical rotation gates	3
II. Experimental setup and device parameters	4
III. Readout optimization of the ancilla qubits	6
A. Quantifying readout error using repeated measurements	6
B. Data qubit idle error during ancilla readout	6
IV. Leakage accumulation during repeated stabilizer measurements	8
V. Bacon-Shor code	9
A. Logical state encoding and measurement	9
B. Logical state preservation	9
C. Logical gates	10
VI. Floquet-Bacon-Shor code	10
A. Logical state encoding and measurement	10
B. Logical state preservation	15
C. Logical Bell states	18
References	21

I. LOGICAL CNOT GATE AND ROTATION GATES IN THE FLOQUET-BACON-SHOR CODE

Here we provide the theoretical derivation of the logical CNOT gate and the logical rotation gates implemented in our experiments. See Methods for operator definitions.

A. Construction of the logical CNOT gate

At round i , the logical CNOT gate between the static and dynamical qubits is defined as

$$\text{CNOT}_L := |0\rangle\langle 0|_s \otimes I_d + |1\rangle\langle 1|_s \otimes X_d^{(i)}.$$

By the equality

$$\text{CNOT}_L = |0\rangle\langle 0|_s \otimes I_d + |1\rangle\langle 1|_s \otimes \left(\Gamma_X^{(i)} X_d \right) = \left(Z_s^{\frac{1-\Gamma_X^{(i)}}{2}} \otimes I_d \right) (|0\rangle\langle 0|_s \otimes I_d + |1\rangle\langle 1|_s \otimes X_d),$$

the implementation of CNOT_L can be decomposed into two parts: (i) $\overline{\text{CNOT}}_L := |0\rangle\langle 0|_s \otimes I_d + |1\rangle\langle 1|_s \otimes X_d$, which can be viewed as using the value of Z_s to control X_d , and (ii) Z_s gate if $\Gamma_X^{(i)} = -1$. We first describe the construction of the nFT circuit for part (i). In our experiment, we implement CNOT_L between stabilizers S_Z^B and S_X^C , where $X_d = X_1 X_7$. To reduce the circuit depth, we use $Z_1 Z_4 Z_7$ as Z_s instead of $Z_2 Z_5 Z_8$. Note that for logical states, operators $Z_1 Z_4 Z_7$ and $Z_2 Z_5 Z_8$ are equivalent because $Z_1 Z_4 Z_7 = S_Z^D \cdot Z_2 Z_5 Z_8$ and S_Z^D does not change logical states. The truth table for $\overline{\text{CNOT}}_L$ is shown in Table S1. From the truth table, we see that the logical CNOT gate can be implemented by applying physical $\text{CNOT}_{4,1}$ and $\text{CNOT}_{4,7}$, and then swapping D_1 and D_7 . Using standard techniques of quantum circuit construction, we obtain the logical CNOT circuit implemented in our experiment. Lastly, part (ii) is conditioned on previous measurement outcomes, which requires real-time feedback control. However, it can be replaced with post-processing, that is, multiplying the logical X and Y measurement outcomes of the static qubit with $\Gamma_X^{(i)}$, because Z_s will flip the logical X and Y measurement outcomes.

Before $\overline{\text{CNOT}}_L$				After $\overline{\text{CNOT}}_L$		
Z_1	Z_4	Z_7	$Z_1 Z_4 Z_7$	Z_1	Z_4	Z_7
+1	+1	+1	+1	+1	+1	+1
+1	+1	-1	-1	-1	+1	+1
+1	-1	+1	-1	-1	-1	-1
+1	-1	-1	+1	+1	-1	-1
-1	+1	+1	-1	+1	+1	-1
-1	+1	-1	+1	-1	+1	-1
-1	-1	+1	+1	-1	-1	+1
-1	-1	-1	-1	+1	-1	+1

TABLE S1. Truth table for $\overline{\text{CNOT}}_L$.

B. Construction of the logical rotation gates

At round i , the logical Z -axis rotation R_Z^θ and X -axis rotation R_X^φ of the dynamical qubit are defined as:

$$\begin{aligned}
R_Z^\theta &:= \exp\left(-i\frac{\theta}{2}Z_d^{(i)}\right) = \exp\left(-i\frac{\Gamma_Z^{(i)}\theta}{2}Z_d\right), \\
R_X^\varphi &:= \exp\left(-i\frac{\varphi}{2}X_d^{(i)}\right) = \exp\left(-i\frac{\Gamma_X^{(i)}\varphi}{2}X_d\right).
\end{aligned}
\tag{S1}$$

The logical rotation gates can be implemented non-fault-tolerantly through the following three steps: (i) Compute the value of Z_d (X_d) on an ancilla qubit by applying a physical CNOT ($\text{CNOT} \cdot (H \otimes I)$) gate between each involved data qubit and the ancilla qubit. (ii) Apply the physical rotation gate $R_z^{\Gamma_Z^{(i)}\theta}$ ($R_x^{\Gamma_X^{(i)}\varphi}$). (iii) Apply the inverse of the circuit used in the first step to disentangle the ancilla qubit.

The implementation of R_Z^θ is more straightforward between stabilizers S_Z^B and S_X^C , because the logical Z operator after stabilizer S_Z^B is $Z_d^{(i)} = \Gamma_Z^{(i)}Z_7Z_8$, and the involved data qubits D_7 and D_8 are physically closer on the square lattice. Similarly, R_X^φ is more easier implemented between stabilizers S_X^C and S_Z^D .

In general, the coefficient $\Gamma_Z^{(i)}$ in the rotation phase $\Gamma_Z^{(i)}\theta$ depends on the outcomes of previous mid-circuit measurements, which typically requires real-time feedback control during the execution of the circuit. In our experiment, the logical R_Z^θ gate is applied to $|+\rangle_d$, and the real-time feedback control can be replaced by data post-processing, as elaborated below.

Using the equality

$$\exp\left(-i\frac{\Gamma_Z^{(i)}\theta}{2}Z_d\right)|+\rangle_d = \frac{e^{-\frac{\Gamma_Z^{(i)}\theta}{2}}|0\rangle_d + e^{\frac{\Gamma_Z^{(i)}\theta}{2}}|1\rangle_d}{\sqrt{2}} = X^{\frac{1-\Gamma_Z^{(i)}}{2}}\exp\left(-i\frac{\theta}{2}Z_d\right)|+\rangle_d,$$

the implementation of R_Z^θ gate on $|+\rangle_d$ can be decomposed into two parts: (i) A logical rotation $\exp(-i\frac{\theta}{2}Z_d)$ that is independent of mid-circuit measurement outcomes, and (ii) A logical X gate if $\Gamma_Z^{(i)} = -1$. Part (ii) can be implemented by data post-processing: since a logical X gate flips the logical Z and Y measurement outcomes, we multiply the measurement outcomes by $\Gamma_Z^{(i)}$. Similarly, when applying the logical R_X^φ gate to state $|0\rangle_d$, we multiply the logical X and Y measurement outcomes by $\Gamma_X^{(i)}$ during data post-processing.

Lastly, achieving universal control of the two-qubit logical state also requires implementing logical rotation gates on the static qubit. By replacing $Z_d^{(i)}$ ($X_d^{(i)}$) with Z_s (X_s) in Eq. (S1), the static logical R_Z^θ (R_X^φ) gate can be non-fault-tolerantly implemented in the same manner as its dynamical counterpart. However, unlike in the dynamical case, the data post-processing is not required, as the state operators remain unchanged during the stabilizer measurement.

II. EXPERIMENTAL SETUP AND DEVICE PARAMETERS

The experiments described in this manuscript are conducted on a superconducting quantum processor comprising 66 qubits and 110 tunable couplers. For details on the chip structure, fabrication process, and packaging scheme, refer to [1] and [2]. A 21-qubit subset of the processor is used in this experiment. The qubit parameters, coherence properties, and gate performance of the subset are summarized in Table S2.

The quantum processor is mounted on the mixing chamber plate of a dilution refrigerator, operating at a temperature of approximately 10 mK. Detailed diagrams of the control electronics, wiring, and filtering are shown in Fig. S1. Custom-made digital-to-analog converter (DAC) and analog-to-digital converter (ADC) circuit boards are used for generating control signals and acquiring data [3]. Integrated bias-tees are employed to combine a shared DC bias signal with qubit/coupler flux pulses. This configuration enables the use of additional attenuators at the DAC ports, which helps suppress low-frequency noise and thereby enhances the Ramsey dephasing time. In the readout line, impedance-matched parametric

Parameters	Mean	Median	Stdev.
Qubit idle frequency (GHz)	4.195	4.223	0.143
Qubit anharmonicity (MHz)	-214.2	-215.0	6.1
Readout frequency (GHz)	6.213	6.218	0.063
T_1 at idle frequency (μ s)	77.2	72.7	17.8
T_2^* at idle frequency (μ s)	3.87	3.85	0.71
T_2^{echo} at idle frequency (μ s)	11.74	11.50	2.85
QND Readout error (% , simultaneous)	1.63	1.58	0.61
Single qubit gate error (% ₀ , simultaneous)	0.76	0.71	0.24
CZ gate error (% , simultaneous)	1.01	0.97	0.30
Dynamical decoupling error (% , simultaneous)	1.46	1.43	0.39

TABLE S2. **Parameters of the superconducting quantum processor.**

amplifiers (IMPAs) [4] are utilized for the initial stage of signal amplification, followed by high electron mobility transistor (HEMT) amplifiers and room-temperature amplifiers. All control signals are routed through multiple stages of attenuation and filtering to prevent noise from entering the quantum processor.

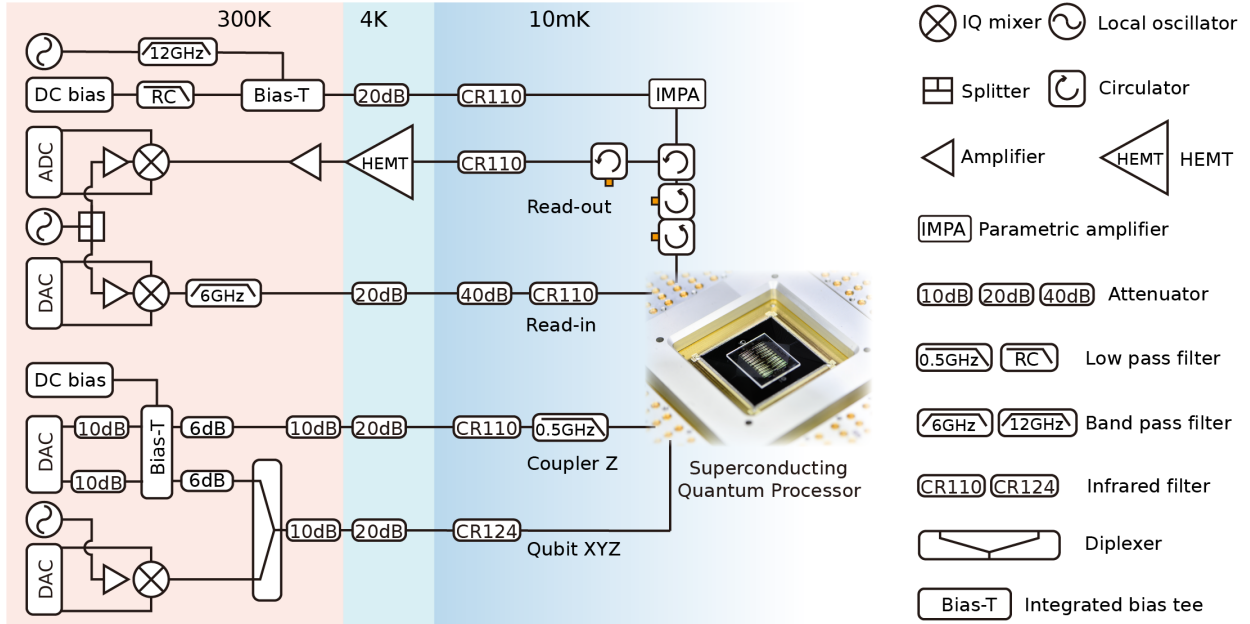


FIG. S1. **Schematic of the experimental setup.**

III. READOUT OPTIMIZATION OF THE ANCILLA QUBITS

A. Quantifying readout error using repeated measurements

To quantify the quantum non-demolition (QND) readout error of an ancilla qubit, we repeatedly perform a composite operation consisting of a readout pulse followed by an R_x^π pulse, with the qubit initialized in a superposition state. The experimental pulse sequence is shown in Fig.S2a. The readout pulse duration is fixed at 500 ns, and a 500 ns delay for resonator photon depletion is inserted between the readout pulse and the R_x^π pulse. The readout error is defined as $\varepsilon_r = 1 - P(0|1)/2 - P(1|0)/2$, where $P(0|1)$ is the probability of measuring the qubit as 0 given that the previous measurement result was 1, and $P(1|0)$ denotes the opposite scenario.

The signal-to-noise ratio (SNR) of the measurement signal is directly related to the readout pulse amplitude A_r . Increasing A_r reduces the separation error $\varepsilon_{\text{sep}} = \frac{1}{2}\text{erfc}(\frac{\sqrt{\text{SNR}}}{2})$. For a given readout pulse, we optimize the demodulation window to maximize the SNR [5]. However, higher readout power may cause state leakage out of the computational subspace [6], leading to an increase in readout error with the number of repeated measurement cycles m , as shown in Fig. S2b. Additionally, higher readout power can induce more cross-measurement dephasing on adjacent data qubits [7]. Since the measurement-induced state transition rate is strongly related to the resonator photon number during readout [8], we set the readout pulse frequency to be centered between the two dressed resonator states. This ensures that the resonator photon number is similar for both qubit states, and the Stark shifts caused by photons in the resonator are also similar. The two dressed resonator states are determined using a kappa-chi-power experiment [9]. The qubit frequency during readout is adjusted by the flux pulse amplitude A_z to avoid two-level system defects, which can cause significant relaxation errors [10]. We optimize the readout error at a fixed number of repeated measurement cycles $m = 10$ by scanning the readout pulse amplitude and the qubit frequency during readout, as shown in Fig. S2c.

B. Data qubit idle error during ancilla readout

The readout pulses and the idle time for resonator photon depletion account for 720 ns, which is approximately 78% of the time spent in a stabilizer round. During the period,

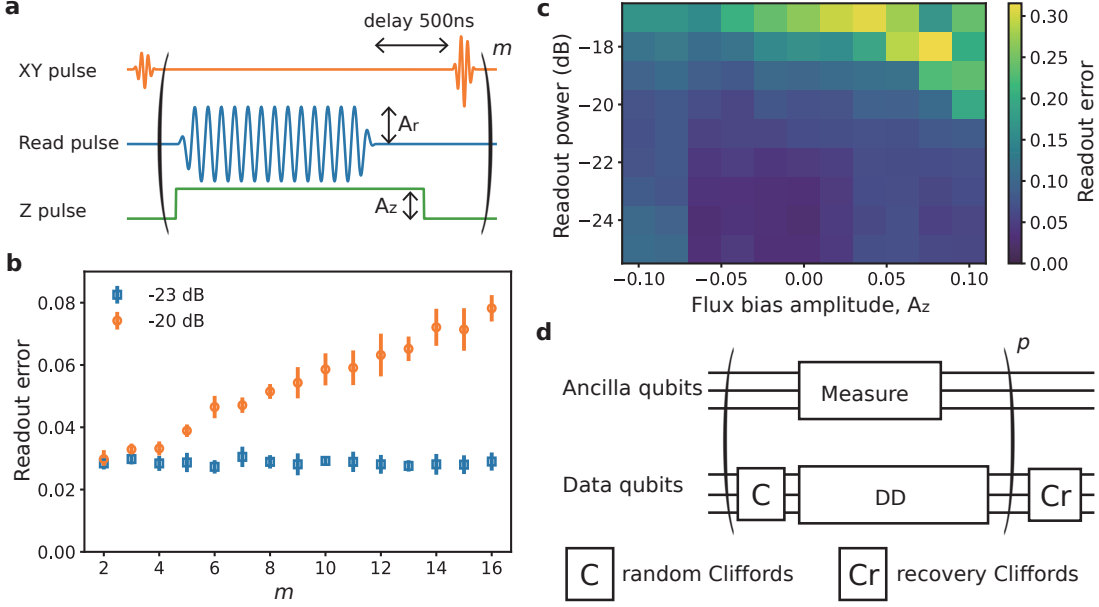


FIG. S2. **Optimizing readout parameters and benchmarking data qubit errors during ancilla readout.** **a**, Experimental sequence for repeated measurements to determine readout errors. The qubit is initialized in a superposition state using an $R_x^{\pi/2}$ pulse before the repeated pulses. A 500 ns delay is inserted between the readout pulse and the $R_x^{\pi/2}$ pulse to deplete residual photons in the resonator. The readout pulse amplitude and frequency, as well as the qubit flux bias amplitude, are optimized to maximize readout fidelity. **b**, Readout error as a function of the number of repeated measurement cycles m for different readout powers. **c**, Readout error as a function of the flux bias amplitude A_z and the readout pulse amplitude (converted to power units), at a fixed number of repeated measurement cycles $m = 10$. **d**, Circuit for the interleaved randomized benchmarking experiment, which measures idle errors of data qubits (with dynamical decoupling pulses) during ancilla qubit readout.

data qubits are subject to energy relaxation and dephasing errors. Additionally, the ancilla qubit measurement process introduces extra phase errors in the data qubits, primarily due to photon crosstalk between readout resonators [11]. To mitigate these dephasing errors, we employ a dynamical decoupling (DD) technique by inserting a Carr-Purcell-Meiboom-Gill (CPMG) sequence [12], consisting of 8 R_y^{π} gates, on the data qubits during the 720 ns measurement time.

We assess the idle errors of the data qubits during ancilla readout using interleaved randomized benchmarking (RB) [13]. The measurement sequence, which includes simultaneous readout pulses on all ancilla qubits and dynamical decoupling sequences on all data qubits, is inserted between single-qubit Clifford gates on the data qubits. The RB circuit is shown in Fig. S2d. The idle error of the data qubits is sensitive to the ancilla qubit frequency

during measurement. To minimize idle errors caused by stray interactions, the ancilla qubit frequency during readout (including Stark shift induced by resonator photons) is adjusted to avoid resonances between the $|10\rangle$ and $|01\rangle$, as well as between $|11\rangle - |20\rangle$ ($|11\rangle - |02\rangle$).

IV. LEAKAGE ACCUMULATION DURING REPEATED STABILIZER MEASUREMENTS

We investigate the accumulation of leakage during state preservation experiments by performing three-state readout on all qubits at the end of multi-round stabilizer measurements. The average leakage populations versus stabilizer rounds for the ancilla and data qubits are shown in Fig. S3. The leakage population p_{leak} increases with the number of stabilizer rounds r , following the relationship: $dp_{\text{leak}}/dr = \epsilon_{\text{leak}} - p_{\text{leak}} \cdot \epsilon_d$, where ϵ_{leak} is the leakage rate per round, and ϵ_d is the average decay rate per round of the second excited states. We fit the leakage data using the function $p_{\text{leak}} = \epsilon_{\text{leak}}/\epsilon_d - (\epsilon_{\text{leak}}/\epsilon_d - p_0) \cdot \exp^{-\epsilon_d r}$, where p_0 is the initial leakage population at round 0. The fitted leakage rates are 0.14% per round for the data qubits and 0.22% per round for the ancilla qubits. The primary source of leakage is attributed to the CZ gates, which involve transitions to the second excited states [14]. The higher leakage rate observed for the ancilla qubits is due to the greater involvement of their second excited states in the implementation of the CZ gates.

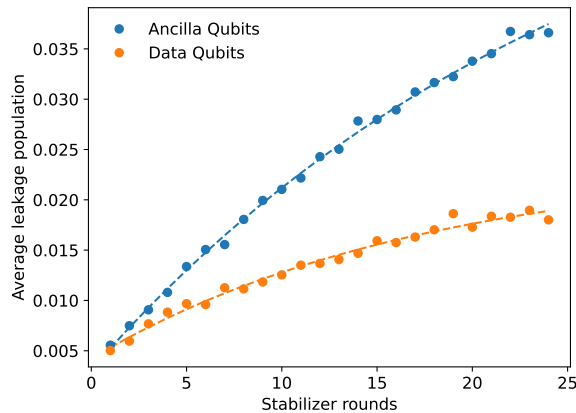


FIG. S3. **Average leakage accumulation on the ancilla (blue) and data (orange) qubits as a function of stabilizer rounds.** The dashed lines indicate exponential fits. The fitted average leakage rates are 0.22% per round for ancilla qubits and 0.14% per round for data qubits.

V. BACON-SHOR CODE

Here we present experimental results for the distance-3 BS code, using the same qubits as in the FBS code. We demonstrate logical state encoding and measurement (Fig. S4), multi-round stabilizer measurements (Fig. S5 and Fig. S6) and FT logical gates (Fig. S7).

A. Logical state encoding and measurement

Logical states $\{|+\rangle, |-\rangle, |0\rangle, |1\rangle\}$ are fault-tolerantly prepared because errors cannot propagate among data qubits arranged in different rows (for $|0\rangle$ and $|1\rangle$) or columns (for $|+\rangle$ and $|-\rangle$). The encoding circuits for $|0\rangle$ and $|+\rangle$ are shown in Fig. S4a. This fault-tolerance does not extend to the state $|+i\rangle$, which requires a more complex encoding circuit. The encoding circuits for $|1\rangle$, $|-\rangle$, and $| -i\rangle$ differ from their counterparts by the addition of logical Pauli gate circuits, as discussed later.

The logical measurement circuit is shown in Fig. S4b. All data qubits are measured simultaneously, enabling final round error detection. The X and Z measurements are FT because the corresponding stabilizers are equivalently performed to detect any single qubit error.

We show the fidelities of the encoded states in Fig. S4c, with error correction and error detection applied to states $\{|+\rangle, |-\rangle, |0\rangle, |1\rangle\}$. The state fidelities are benchmarked using single-qubit LQST. The near-unity fidelities achieved with error detection indicate that most errors has been successfully detected within the BS code. In contrast, error detection or error correction are not performed for the states $|\pm i\rangle$ due to the nFT nature of the logical Y measurement.

B. Logical state preservation

In the conventional BS code, X and Z stabilizer measurements are performed alternatively in a 2D grid, with the four central qubits alternatively used as X and Z ancilla qubits. Here, we merge the X and Z stabilizers into a single stabilizer round using extra ancilla qubits. Consequently, each stabilizer round consists of four weight-6 stabilizers (two X stabilizers and two Z stabilizers). The corresponding circuit is shown in Fig. S5. We present the results of logical state preservation for encoded states $\{|+\rangle, |-\rangle, |0\rangle, |1\rangle\}$ in Fig. S6. An error

detection event occurs when any stabilizer measurement result deviates from its theoretical value. Stabilizer measurement results are compared to those from the previous round, except for the first and last rounds. A lower detection probability is observed in the first (last) round because data qubit initialization (measurement) values are used to identify parity errors and generate detection events. A slight increase in detection probability is observed in the intermediate rounds, likely due to the accumulation of leakage errors.

Notably, we do not apply reset operations to the ancilla qubits between stabilizer rounds. Instead, we perform XOR operations on the measurement results of the ancilla qubits during post-processing [15]. Due to the exponential drop in the retained rate for error detection, we limit our analysis to five rounds, with each experiment comprising 10,000 measurement shots.

C. Logical gates

The FT logical gates are implemented transversally by applying parallel single qubit rotation gates on relevant data qubits. The gate circuits for the logical X , Y , Z , and $Y(\pi/2)$ gates are shown in Fig. S7a. The $Y(\pi/2)$ gate is implemented by applying $R_y^{\pi/2}$ gates on all the data qubits and reassigning the data qubit indices during post-processing. We insert the transversal gates between two integrated stabilizer rounds and perform LQST on the final states, as shown in Fig. S7b. The infidelities of the final-states, averaged over 4 encoded states $\{|0\rangle, |1\rangle, |+\rangle, |-\rangle\}$, are compared to the infidelity of the identity gate (i.e., with no gate inserted), as shown in Fig. S7c. To assess the performance of the logical gates with error detection, we perform LQST using six logical cardinal states $\{|0\rangle, |1\rangle, |+\rangle, |-\rangle, |+i\rangle, |-i\rangle\}$ as input states. The LPTMs extracted from over-complete sets of input-output logical-state pairs are shown for the X , Y , Z , $Y(\pi/2)$ gates in Fig. S7d.

VI. FLOQUET-BACON-SHOR CODE

A. Logical state encoding and measurement

We present the encoding circuits for 36 Pauli states in Fig. S8a. The states in the subgroup $\{|0\rangle, |1\rangle, |+\rangle, |-\rangle\}^{\otimes 2}$ are fault-tolerantly prepared. Pauli states with the static and dynamical qubits in different bases, as $\{|0, +/\rangle, |1, +/\rangle, |+, 0/1\rangle, |-, 0/1\rangle\}$, are products

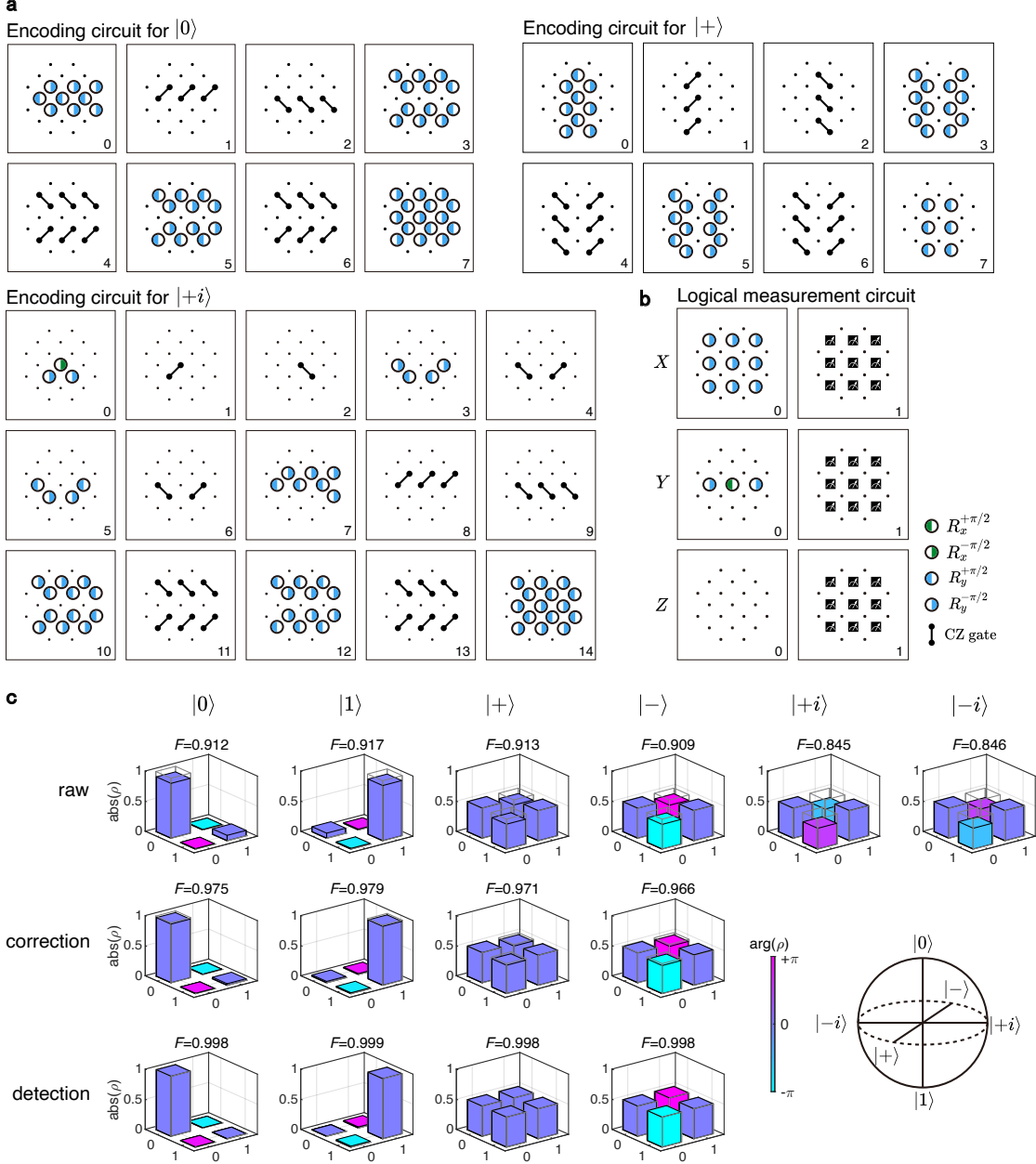


FIG. S4. **Encoding logical states in the BS code.** **a**, Encoding circuits for logical states $|0\rangle$, $|+\rangle$, and $|+i\rangle$, with the gate patterns arranged in order (numbered at the bottom-right corner). **b**, Logical measurement circuits for the BS code: X (top), Y (middle), and Z (bottom). **c**, LQST results for encoded Pauli states: without post-processing (top), with error correction (middle), and with error detection (bottom). The wireframes represent the amplitudes of the ideal density matrices.

of GHZ states. The state $|+,0\rangle$ differs from $|0,+\rangle$ by entangling data qubits in rows or columns. In the latter case, physical $R_y(-\pi/2)$ gates are applied to all data qubits after the entangling circuit. The remaining states in the group are encoded by applying additional

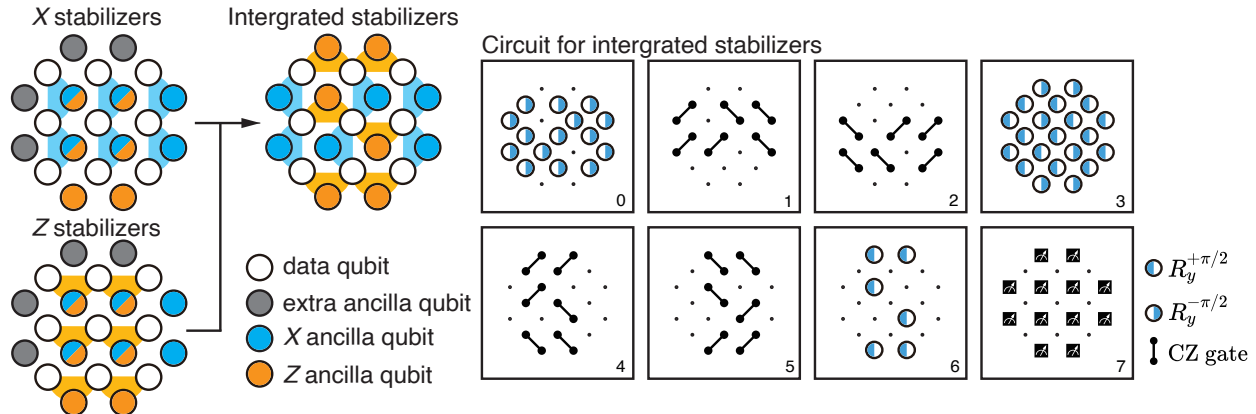


FIG. S5. **Integrating X and Z stabilizers in the BS code.** We introduce additional ancilla qubits (grey circles) on the left and top of the lattice to combine the X and Z stabilizers into a single stabilizer round for the distance-3 BS code, as indicated by the arrow. Each stabilizer round now includes four weight-6 stabilizers: two X stabilizers and two Z stabilizers. The detailed circuit for the integrated stabilizer is shown on the right.

logical X or Z gates to either the static or dynamical qubit. The corresponding gate circuits are shown in Fig. S8b. For Pauli states with both the static and dynamical qubits in the X (Z) basis, the state of the dynamical qubit depends on the outcome of the previous X (Z) stabilizer measurement.

Two-qubit states involving $|\pm i\rangle$ are prepared in a nFT manner. The static qubit is encoded into the $|\pm i\rangle$ state by first setting $Y_s = \pm 1$ (the corresponding circuits are illustrated in Fig. S8c) and then projecting the system onto the logical subspace via BS stabilizer measurements. However, all four stabilizers take on random initial values, preventing their use for error detection. The dynamical qubit is encoded into the $|\pm i\rangle$ state using Y_d -basis measurements, with logical states post-selected. To reduce circuit depth, instead of measuring Y_d directly, we decompose it at round A into two gauge operators $Y_d = Y_1 Z_3 X_4 = Y_1 X_4 Z_2 \cdot Z_2 Z_3$ and then measure $Y_1 X_4 Z_2$ and $Z_2 Z_3$ separately (measurement circuit illustrated in Fig. S8d). If the product of these two measurement outcomes is $+1$ (-1), the logical state will be projected onto $|i\rangle_d$ ($|-i\rangle_d$) by the subsequent stabilizer measurement round S_X^A . This process is also nFT due to the inherently nFT nature of the logical Y measurement.

Physical rotation gates are applied to the data qubits before the readout pulses to measure the relative logical operators for the dynamical (left) and static (right) qubits, are shown in Fig. S9. The circuit for the dynamical qubit varies according to the type of preceding stabilizer. The circuits for the static and dynamical logical qubits can be combined to perform

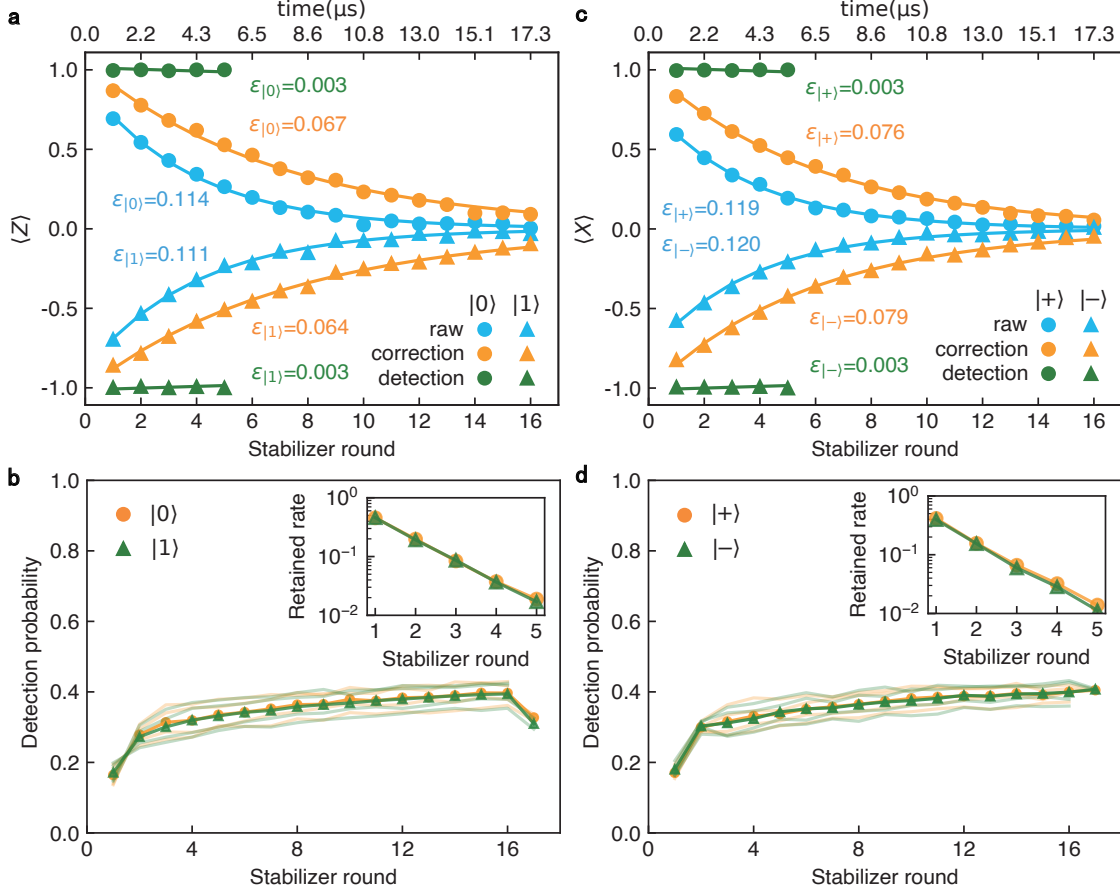


FIG. S6. **Logical state preservation in the BS code with integrated X and Z stabilizer measurements.** **a**, Measured expectation values of the logical Z operator versus stabilizer round for prepared $|0\rangle$ (circles) and $|1\rangle$ (triangles). The cyan, green, and orange colors correspond to data without post-processing, data with error detection, and data with error correction, respectively. Solid lines represent exponential fits. **b**, Detection probability for each weight-6 stabilizer over 16 rounds of stabilizer measurements, for encoded states $|0\rangle$ (orange) and $|1\rangle$ (green). Darker lines show the average detection probabilities for the two encoded states. Detection probabilities are lower in the first and last rounds, where data qubit initialization and measurement values are used to identify parity errors. A slight increase in detection probability is observed in the intermediate rounds, likely due to accumulated leakage errors. The inset shows the exponential decrease in the retained data rate during error detection, based on 10,000 experimental shots, with corresponding exponential fits (solid lines). **c** and **d**, Same as **a** and **b**, but for logical states $|+\rangle$ and $|-\rangle$.

simultaneous logical measurements on both qubits. We present the logical measurement circuits for 9 logical bases after the stabilizer round S_X^D in Fig. S10. Data qubits that do not participate in defining the logical operators are measured to detect errors in the final round.

The encoded state fidelities of the 36 Pauli states are summarized in Table S3, with and without error detection during logical measurement. The fidelities are benchmarked used LQST. Error detection shows negligible improvement for $|\pm i, \pm i\rangle$ states because no stabilizer

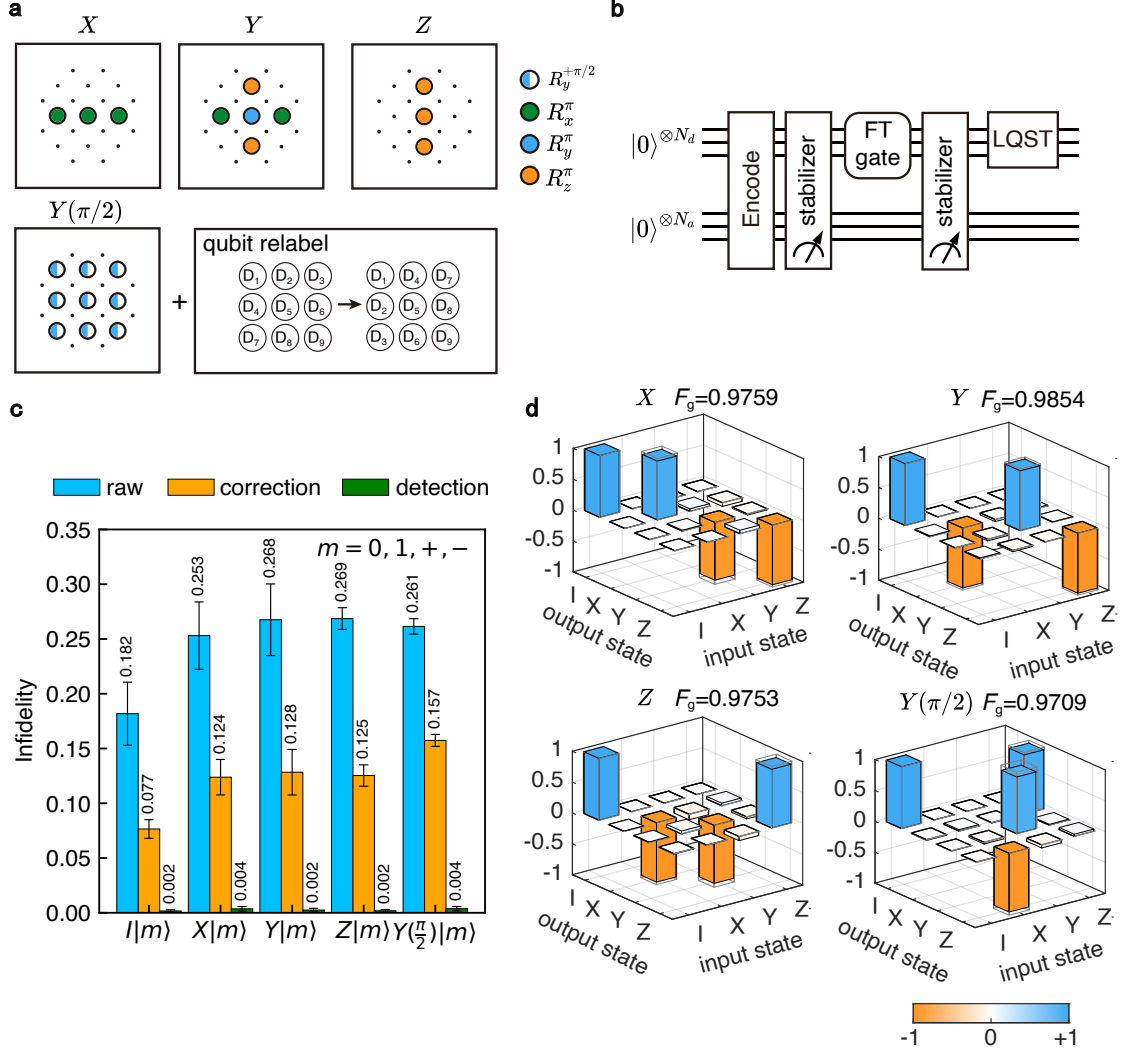


FIG. S7. **Logical gates in the BS code.** **a**, Circuits for the logical X , Y , Z and $Y(\pi/2)$ gate. The $Y(\pi/2)$ gate is implemented by applying physical $R_y^{\pi/2}$ gates on all the data qubits and relabeling the data qubit indices in post-processing. **b**, Circuit for implementing the FT logical gates in the BS code. The transversal gates on the data qubits are inserted between two integrated stabilizers, and LQST is used to determine the final state fidelity. **c**, Average state infidelities over four encoded states after applying the respective logical gates and two stabilizer rounds, without post-processing (blue), with error detection (green) and with error correction (orange). Error bars correspond to 95% confidence intervals. For the identity gate, no gate circuit is inserted, and only one stabilizer round is applied after the encoding circuit. **d**, Constructed LPTMs for the X , Y , Z and $Y(\pi/2)$ gates, with error detection applied to both the input states and output states. Both the input and output states are characterized using LQST.

values can be calculated from the $Y_s Y_d$ measurement outcomes.

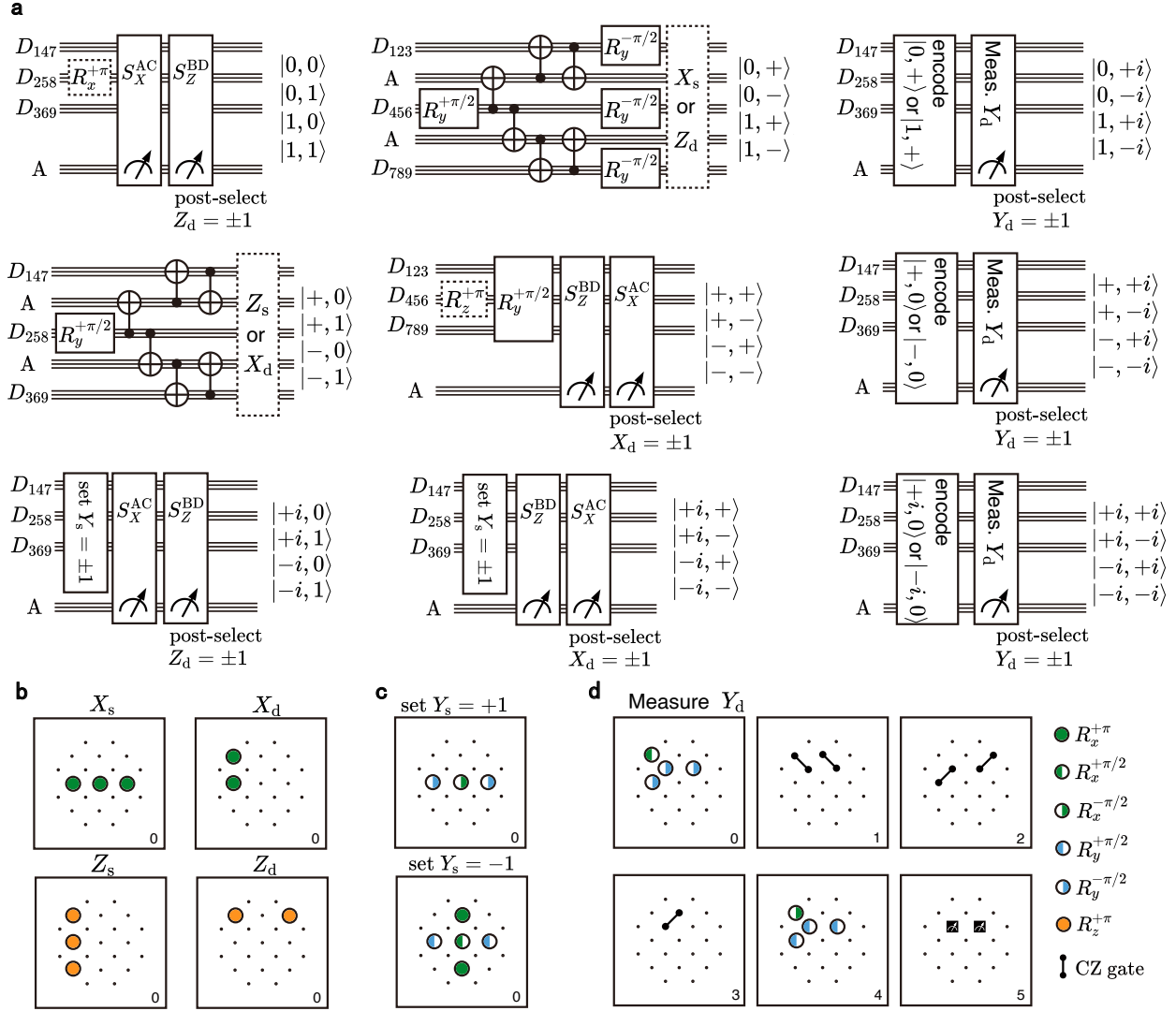


FIG. S8. **Encoding circuits for Pauli states in the FBS code.** **a**, Encoding circuits for 36 Pauli states. The 16 states in the group $\{|0\rangle, |1\rangle, |+\rangle, |-\rangle\}^{\otimes 2}$ are fault-tolerantly prepared. The dashed box indicates the gate circuit for FT Pauli gates on the data qubits, detailed in **b**. **b**, Circuits for logical X (top) and Z (bottom) gates applied to the static (left) and dynamical (right) qubits. **c**, Circuits for setting the Y_s operator of the static qubit to $+1$ (top) and -1 (bottom). **d**, Circuit for setting the Y_d operator of the dynamical qubit using ancilla measurements. The dynamical qubit is set to $|+i\rangle$ ($|-i\rangle$) if the measured parity of the two ancilla qubits is $+1$ (-1).

B. Logical state preservation

The state preservation results for the static and dynamical qubit with encoded states $|+, 0\rangle, |+, 1\rangle, |-, 0\rangle, |-, 1\rangle$ are shown in Fig. S11, showing the measured expectation values for the X_s operator of the static qubit (left column) and the Z_d operator of the dynamical qubit (middle column).

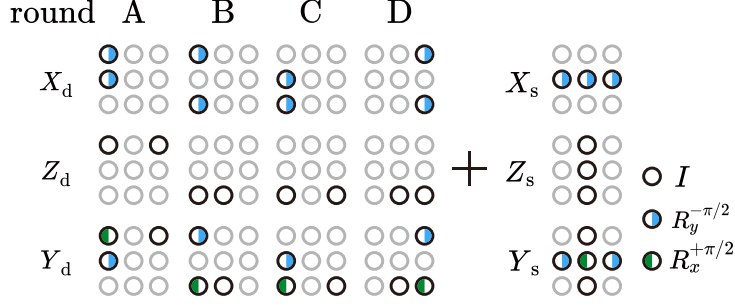


FIG. S9. **Physical rotation gates applied to the data qubits before readout pulses for measuring logical operators.** The rotation gates for the logical operators of the dynamical and static qubits are combined to enable simultaneous logical measurements. The rotation gates for the dynamical qubit's operators varies according to the type of preceding stabilizer.

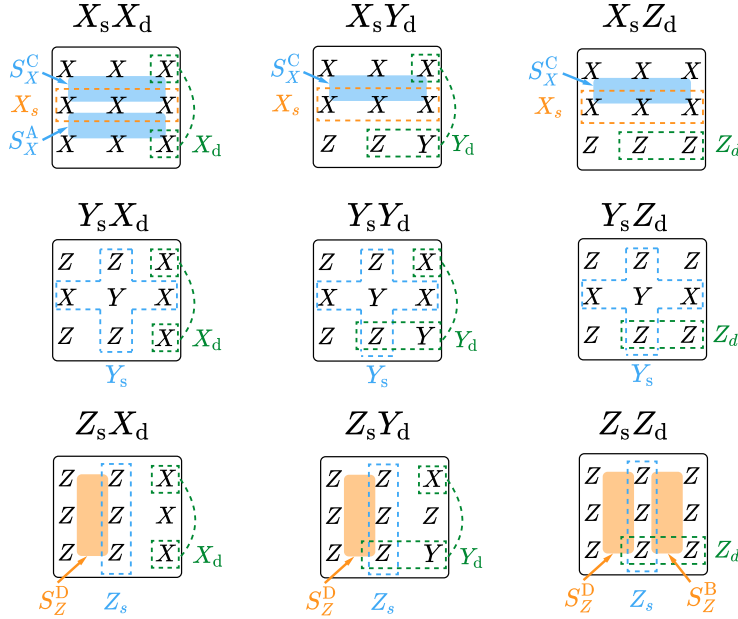


FIG. S10. **Two-qubit logical measurement circuits in 9 bases after stabilizer S_X^D .** The $X_s X_d$ and $Z_s Z_d$ operators are fault-tolerantly measured, with two stabilizer values are calculated to detect any single-qubit error. Although measurements of $X_s Y_d$, $X_s Z_d$, $Z_s X_d$, and $Z_s Y_d$ are not FT, some errors can still be detected by a single stabilizer.

In the period-4 stabilizer measurements, each measurement result is compared to the result of the same stabilizer type from four rounds prior, except for the first four rounds and the last round. The measurement results of the first four stabilizer rounds are compared to the initial values determined by the encoding process. In the last round, error detection probability is calculated from the measurement results of the data qubits. The corresponding error detection probabilities are shown on the right of Fig. S11, with the insets displaying

Encoded state	Fidelity (raw)	Fidelity (detection)	Fault-tolerance	Encoded state	Fidelity (raw)	Fidelity (detection)	Fault-tolerance
$ 0, 0\rangle$	0.775	0.898	FT	$ +i, 0\rangle$	0.687	0.763	nFT
$ 0, 1\rangle$	0.771	0.897	FT	$ +i, 1\rangle$	0.679	0.756	nFT
$ 1, 0\rangle$	0.762	0.891	FT	$ -i, 0\rangle$	0.703	0.767	nFT
$ 1, 1\rangle$	0.770	0.896	FT	$ -i, 1\rangle$	0.685	0.761	nFT
$ 0, +\rangle$	0.847	0.949	FT	$ 0, +i\rangle$	0.696	0.831	nFT
$ 0, -\rangle$	0.832	0.949	FT	$ 0, -i\rangle$	0.706	0.845	nFT
$ 1, +\rangle$	0.841	0.948	FT	$ 1, +i\rangle$	0.717	0.843	nFT
$ 1, -\rangle$	0.847	0.946	FT	$ 1, -i\rangle$	0.730	0.848	nFT
$ +, 0\rangle$	0.805	0.931	FT	$ +, +i\rangle$	0.626	0.754	nFT
$ +, 1\rangle$	0.799	0.927	FT	$ +, -i\rangle$	0.611	0.715	nFT
$ -, 0\rangle$	0.786	0.923	FT	$ -, +i\rangle$	0.610	0.738	nFT
$ -, 1\rangle$	0.784	0.919	FT	$ -, -i\rangle$	0.614	0.736	nFT
$ +, +\rangle$	0.752	0.878	FT	$ +i, +\rangle$	0.717	0.782	nFT
$ +, -\rangle$	0.756	0.879	FT	$ +i, -\rangle$	0.718	0.777	nFT
$ -, +\rangle$	0.745	0.878	FT	$ -i, +\rangle$	0.697	0.751	nFT
$ -, -\rangle$	0.744	0.871	FT	$ -i, -\rangle$	0.683	0.735	nFT
				$ +i, +i\rangle$	0.555	0.562	nFT
				$ +i, -i\rangle$	0.544	0.550	nFT
				$ -i, +i\rangle$	0.552	0.557	nFT
				$ -i, -i\rangle$	0.561	0.564	nFT

TABLE S3. Fidelities of 36 encoded Pauli states in the FBS code, measured with and without error detection using LQST.

the exponential decrease in the retained data rate during error detection. Due to the lack of reset operations between stabilizer rounds, we perform XOR operations on the measurement results of the ancilla qubits during post-processing.

Taking the encoded state $|+, 0\rangle$ as an example, the logical error rate of the static qubit is significantly reduced through error detection. Specifically, the error rate is suppressed from 8.0% to 0.3% by fitting the exponential decay of the expectation values. This improvement corresponds to an increase in the logical lifetime from $5.8 \mu\text{s}$ to $153 \mu\text{s}$. The logical lifetime with error detection surpasses the average coherence time $T_2^E = 12.5 \mu\text{s}$ of the physical qubits. In contrast, the dynamical qubit exhibits a shorter logical lifetime due to reduced protection. With error detection, the logical error rate for the dynamical qubit is suppressed from 10.6% to 3.0%, corresponding to an increase in the logical lifetime from $4.3 \mu\text{s}$ to $15.3 \mu\text{s}$. This difference arises because the static qubit requires three single-qubit errors to cause a logical

error, whereas the dynamical qubit can experience a logical error with only two single-qubit errors.

Beyond error detection, error correction can be performed on the static qubit alone, as it can be viewed as a BS code of distance 3. We decode the measured error syndromes using minimum-weight perfect matching algorithm [16]. For encoded state $|+, 0\rangle$, error rate of the error-corrected static qubit is 5.8%, corresponding to a logical lifetime of 8.3 μ s. However, the effectiveness of such error correction diminishes for the joint two-qubit states due to insufficient code distance and the correlation between errors in the two logical qubits. We present error detection results for the two-qubit logical states in Fig. S12, using the same data as in Fig. S11.

C. Logical Bell states

We present the LQST results for four logical Bell states in Fig. S13. The measured fidelities of the states $\frac{1}{\sqrt{2}}(|0, 0\rangle + |1, 1\rangle)$, $\frac{1}{\sqrt{2}}(|0, 1\rangle + |1, 0\rangle)$, $\frac{1}{\sqrt{2}}(|0, 0\rangle - |1, 1\rangle)$, and $\frac{1}{\sqrt{2}}(|0, 1\rangle - |1, 0\rangle)$ with error detection are 0.759, 0.753, 0.721, 0.757, respectively. Without error detection, the corresponding fidelities are 0.388, 0.369, 0.375, and 0.385.

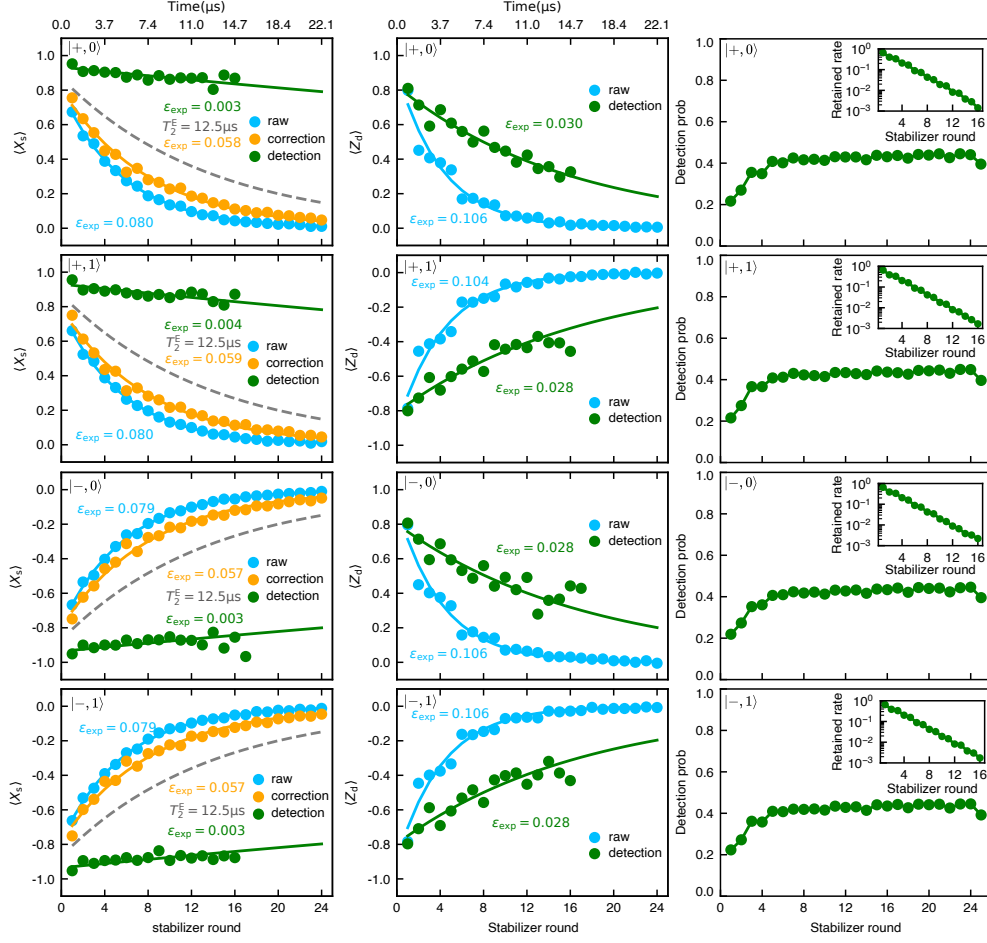


FIG. S11. **Logical state preservation in the FBS code.** Multi-round state preservation results for the static qubit (left column) and the dynamical qubit (middle column), with different encoded states in each row. Each stabilizer round lasts 920 ns, comprising 720 ns for readout pulses and resonator photon depletion, and 200 ns for single-qubit and two-qubit gates. The cyan, green, and orange dots correspond to data without post-processing, with error detection, and with error correction, respectively. The average spin-echo dephasing time $T_2^E = 12.5 \mu s$ of the physical qubits is shown as a dashed line for comparison. The corresponding error detection probabilities are shown in the right column, with the inset displaying the exponential decrease in the retained data rate during error detection, based on a total of 100,000 experimental shots.

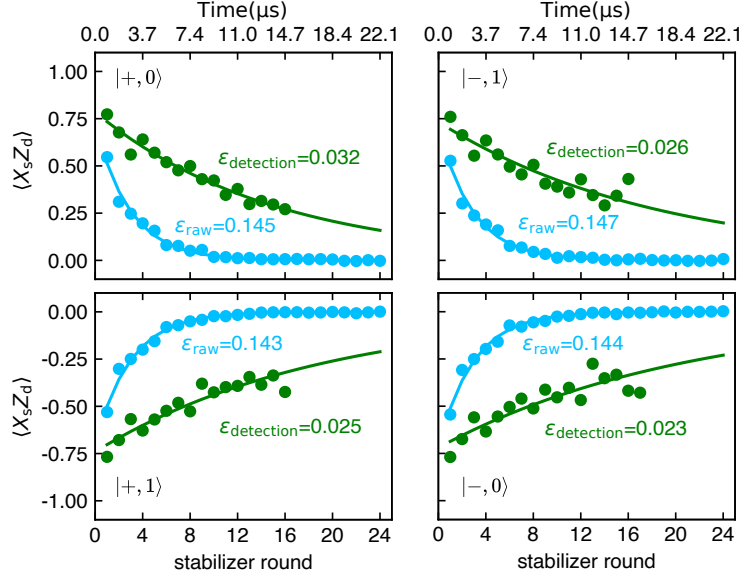


FIG. S12. **Logical state preservation results for two-qubit states in the FBS code.** The cyan and green dots correspond to the data without post-processing and with error-detection, respectively. The data are the same as those in Fig. S11.

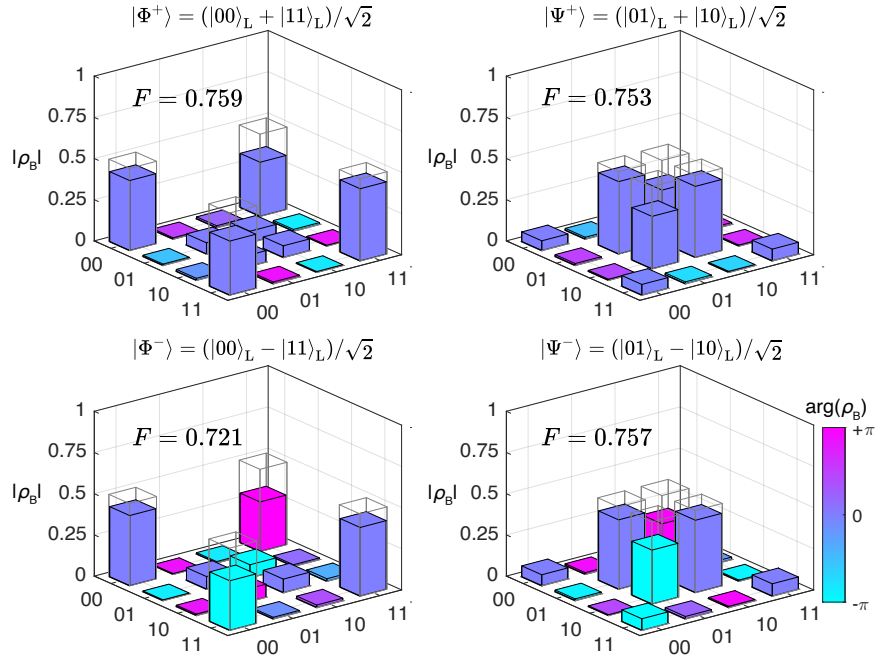


FIG. S13. **Logical Bell states.** LQST results of four Bell states $\{|\Phi^+\rangle, |\Psi^+\rangle, |\Phi^-\rangle, |\Psi^-\rangle\}$ generated from encoded states $\{|+, 0\rangle, |+, 1\rangle, |-, 0\rangle, |-, 1\rangle\}$ in the FBS code. The fidelities with error detection are shown.

-
- [1] Yang, X. *et al.* Coupler-assisted leakage reduction for scalable quantum error correction with superconducting qubits. *Physical Review Letters* **133**, 170601 (2024).
- [2] Huang, W. *et al.* Exact quantum critical states with a superconducting quantum processor. *arXiv preprint arXiv:2502.19185* (2025).
- [3] Zhang, J. *et al.* M² CS: A microwave measurement and control system for large-scale superconducting quantum processors. *Chin. Phys. B* **33**, 120309 (2024).
- [4] Mutus, J. Y. *et al.* Strong environmental coupling in a josephson parametric amplifier. *Applied Physics Letters* **104** (2014).
- [5] Bengtsson, A. *et al.* Model-based optimization of superconducting qubit readout. *Physical Review Letters* **132**, 100603 (2024).
- [6] Sank, D. *et al.* Measurement-induced state transitions in a superconducting qubit: Beyond the rotating wave approximation. *Physical Review Letters* **117**, 190503 (2016).
- [7] Bultink, C. *et al.* Protecting quantum entanglement from leakage and qubit errors via repetitive parity measurements. *Science Advances* **6**, eaay3050 (2020).
- [8] Hazra, S. *et al.* Benchmarking the readout of a superconducting qubit for repeated measurements. *arXiv preprint arXiv:2407.10934* (2024).
- [9] Sank, D. *et al.* System characterization of dispersive readout in superconducting qubits. *Physical Review Applied* **23**, 024055 (2025).
- [10] Thorbeck, T., Xiao, Z., Kamal, A. & Govia, L. C. Readout-induced suppression and enhancement of superconducting qubit lifetimes. *Physical Review Letters* **132**, 090602 (2024).
- [11] Szombati, D. *et al.* Quantum rifling: Protecting a qubit from measurement back action. *Physical Review Letters* **124**, 070401 (2020).
- [12] Meiboom, S. & Gill, D. Modified spin-echo method for measuring nuclear relaxation times (1958).
- [13] Magesan, E. *et al.* Efficient measurement of quantum gate error by interleaved randomized benchmarking. *Physical Review Letters* **109**, 080505 (2012).
- [14] Sung, Y. *et al.* Realization of high-fidelity cz and zz-free iswap gates with a tunable coupler. *Physical Review X* **11**, 021058 (2021).

- [15] Kelly, J. *et al.* State preservation by repetitive error detection in a superconducting quantum circuit. *Nature* **519**, 66–69 (2015).
- [16] Fowler, A. G., Mariantoni, M., Martinis, J. M. & Cleland, A. N. Surface codes: Towards practical large-scale quantum computation. *Physical Review A—Atomic, Molecular, and Optical Physics* **86**, 032324 (2012).